A FFT-based numerical implementation of mesoscale field dislocation mechanics: Application to two-phase laminates

Komlan Djaka, Stéphane Berbenni, Vincent Taupin, Ricardo A Lebensohn

HAL Id: hal-02352968

https://hal.science/hal-02352968

Submitted on 7 Nov 2019

A FFT-based numerical implementation of mesoscale field dislocation mechanics: application to two-phase laminates

Komlan S. Djaka [a,c], Stéphane Berbenni [a,c,1],

Vincent Taupin [a,c], Ricardo A. Lebensohn [b]

[a] *Université de Lorraine, Arts et Métiers Paris Tech, CNRS, LEM3, F-57000 Metz, France*

[b] *Theoretical Division, Los Alamos National Laboratory, Los Alamos, NM 87845, USA*

[c] *Laboratory of Excellence on Design of Alloy Metals for low-mAss Structures (DAMAS), Université de Lorraine, France*

Abstract

In this paper, we present an enhanced crystal plasticity elasto-viscoplastic fast Fourier transform (EVPFFT) formulation coupled with a phenomenological Mesoscale Field Dislocation Mechanics (MFDM) theory here named MFDM-EVPFFT formulation. In contrast with classic CP-EVPFFT, the model is able to tackle plastic flow and hardening due to polar dislocation density distributions or geometrically necessary dislocations (GNDs) in addition to statistically stored dislocations (SSDs). The model also considers GND mobility through a GND density evolution law numerically solved with a recently developed filtered spectral approach, which is here coupled with stress equilibrium. The discrete Fourier transform method combined

with finite differences is applied to solve both lattice incompatibility and Lippmann-Schwinger equations in an augmented Lagrangian numerical scheme. Numerical results are presented for two-phase laminate composites with plastic channels and elastic second phase. It is shown that both GND densities and slip constraint at phase boundaries influence the overall and local hardening behavior. In contrast with the CP-EVPFFT formulation, a channel size effect is predicted on the shear flow stress with the present MFDM-EVPFFT formulation. The size effect originates from the progressive formation of continuous screw GND pile-ups from phase boundaries to the channel center. The effect of GND mean free path on local and global responses is also examined for the two-phase composite.

Keywords: dislocations; crystal plasticity; two-phase composites; Mesoscale Field Dislocation Mechanics; FFT; elastoviscoplastic material

1   Introduction

Many efforts have been made in the past to predict the size dependence of mechanical material's response during the transition from millimeter to micron or sub micron material length scales. Generally, size effects are due non local effects inherent to strain/slip gradients and usually manifest as an increase of the flow strength of the material with diminishing the characteristic size of the microstructure (i.e. grain size, particle size...). For example, in dispersion-hardened alloys, it was observed that the flow strength of the composite material increases as the average particle size and the average particle spacing decrease (Ashby, 1970; Lloyd, 1994; Nan and Clarke, 1996). Therefore, to deal with such size effects, different strain

---

[1] Corresponding author.

Email address: `stéphane.berbenni@univ-lorraine.fr` (Stéphane Berbenni)

gradient plasticity theories have been developed during the last decades (Aifantis, 1984, 1987; Mülhaus and Aifantis, 1991; Fleck and Hutchinson, 1993, 1997; Gao et al., 1999; Fleck and Hutchinson, 2001; Bassani, 2001; Gurtin, 2000, 2002, 2004; Gudmundson, 2004; Gurtin and Anand, 2005, 2009; Fleck and Willis, 2009; Fleck et al., 2015). Strain gradient plasticity theories were also coupled with crystal plasticity theories incorporating both SSDs (statistically stored dislocations) and GNDs (geometrically necessary dislocations) (Arsenlis and Parks, 1999, 2002; Acharya and Bassani, 2000; Acharya and Beaudoin, 2000; Evers et al., 2002, 2004; Gurtin et al., 2007; Han et al., 2005; Cordero et al., 2010, 2012; Wulfinghoff et al., 2015). Size dependent material behaviors can also be predicted by discrete methods like Discrete Dislocation Dynamics (DDD) and comparisons between DDD and strain gradient plasticity theories were reported (Shu et al., 2001; Bassani et al., 2001; Bittencourt et al., 2003; Danas et al., 2010; Chang et al., 2015). From the continuum and mathematical point of view, dislocations were introduced by Volterra (1907). The state of elastic incompatibility due to dislocations was described smoothly in the elastic theory of continuously distributed dislocations (ECDD) through the use of the Nye's dislocation density tensor (Nye, 1953; Kröner, 1958; Fox, 1966; Willis, 1967; Eisenberg, 1970; Ashby, 1970; Han and Jaunzemis, 1973; Kosevich, 1979; Kröner, 1981). ECDD was recently revisited by Acharya (2001, 2003, 2004) through the so-called Field Dislocation Mechanics theory (FDM). A recently proposed continuum approach, called Phenomenological Mesoscopic Field Dislocation Mechanics (hereafter abbreviated MFDM) was seen to be successful in modeling different problems in plasticity at mesoscopic scale and small strains (Acharya and Roy, 2006; Acharya et al., 2006; Roy and Acharya, 2006). This theory can be seen as a combination of field dislocation mechanics theory (Acharya, 2001, 2003; Roy and Acharya, 2005) and strain gradient crystal plasticity at small strains integrating the mobilities of both GNDs and SSDs (Acharya and Roy, 2006). A comparison of the MFDM theory

(full and reduced versions) with lower order strain gradient crystal plasticity models were provided in Roy et al. (2007). In this mesoscale theory, the constitutive equations for strain-hardening models, slip rule for SSDs and velocity of GNDs need to be specified phenomenologically, but it allows performing simulations at reasonable strain rates compared to DDD. Transport of GND density was numerically solved by the Finite Element (FE) method in Roy and Acharya (2005, 2006) and in Varadhan et al. (2006). Different size effects for single crystalline materials and multicrystalline thin films have been predicted with the MFDM theory as reported in Roy and Acharya (2006), Puri et al. (2009) and Puri et al. (2011). Grain size distribution and crystallographic orientation effects in multicrystalline thin films were discussed in Puri and Roy (2012). Using the MFDM theory, Taupin et al. (2008) examined the role of GNDs on the directionality of yield stress in strain-aged steels. The role of the transport of GNDs in ice single- or multi-crystals was highlighted in Taupin et al. (2007) and Richeton et al. (2017). Varadhan et al. (2009) and Gupta et al. (2017) coupled the MFDM equations with a dynamic strain aging (DSA) model in order to predict the strain-aging behaviors of single crystalline and polycrystalline Al alloys. Regarding non local theories for grain boundaries as obstacles to crystallographic slip, different formulations have been developed this last decade to describe grain boundaries as being impenetrable or penetrable to slip and dislocations (Gurtin and Needleman, 2005; Aifantis and Willis, 2005; Acharya, 2007; Pardoen and Massart, 2012). Among these formulations, Acharya (2007) formulated a jump condition at a material interface, like a phase or a grain boundary, adapted for both the FDM and the MFDM theories based on the conservation of Burgers vector. For a fixed interface, this condition states a tangential continuity of the plastic distortion rate which has consequences on interfacial GND content and slip. Such continuity constraints at material interfaces were seen to have consequences on the mechanical responses of bicrystals (Puri et al., 2010), multicrystalline thin flims (Puri et al., 2011) and

4

metal matrix composites (Richeton et al., 2011; Taupin et al., 2012).

Micromechanical models for heterogeneous materials require solving partial differential equations (PDEs) with appropriate constitutive equations and boundary conditions. Polycrystal plasticity models can be formulated and numerically implemented using finite elements (FE) for the solution of the governing PDEs combined with crystal plasticity (CP) constitutive descriptions at the level of each single crystal material point in the FE discretization (Mika and Dawson, 1998; Delaire et al., 2000; Barbe et al., 2001; Cailletaud et al., 2003; Roters et al., 2010). However, the large number of degrees of freedom may limit the size of the polycrystalline microstructures that can be simulated with FE. An efficient spectral alternative to CP-FE based on computationally efficient fast Fourier transform (FFT) algorithm, originally proposed by Moulinec and Suquet (1994, 1998) for composites, was extended by Lebensohn (2001) to solve the micromechanical behavior of polycrystals. This formulation solves, for periodic unit cells, the PDEs associated with stress equilibrium and strain compatibility. This solution is obtained from convolution integrals involving the periodic Green's function associated with the displacement field of a homogeneous linear reference medium, and a stress polarization field that contains all the information of the materials heterogeneity and non-linearity. The material properties and micromechanical response are given at each point in a regular and periodic grid. With this discretization, and applying fast Fourier transform (FFT) to those convolution integrals, their computation is replaced by simple products in Fourier space, which, in turn, are anti-transformed back to Cartesian space. An iterative procedure involving these back-and-forth transformations between Fourier and Cartesian spaces is generally required to converge to strain and stress fields satisfying compatibility and equilibrium, respectively, as well as the constitutive relation at each grid point. In Moulinec-Suquet original FFT-based basic scheme (Moulinec and

Suquet, 1994, 1998), the solution is obtained using a fixed-point iterative algorithm. The contrast in local mechanical properties of the heterogeneous material affects the convergence rate of the method, with higher contrast requiring more iterations to achieve convergence. The properties of the linear reference material do not change the predicted micromechanical fields, but do affect the convergence rate, as well. Since its inception, several improvements to the basic scheme have been proposed (Eyre and Milton, 1999; Michel et al., 2001; Brisard and Dormieux, 2010, 2012; Monchiet and Bonnet, 2013; Kabel et al., 2014; Schneider, 2017), based on modifications of the iterative algorithm to accelerate convergence. FFT-based methods were initially developed and applied to composite materials (Moulinec and Suquet, 1994, 1998; Eyre and Milton, 1999; Michel et al., 2001), in which the heterogeneity is given by the spatial distribution of phases with different mechanical properties, and later adapted to polycrystals (Lebensohn, 2001), where the heterogeneity is related to the spatial distribution of anisotropic crystals with different orientations. This original CP-FFT implementation showed the feasibility of efficiently solving the micromechanical behavior of complex polycrystalline unit cells. Subsequent numerical implementations of the FFT-based method for polycrystals have been developed, for different constitutive descriptions of the behavior of each single crystal material point. For polycrystals, the different constitutive regimes solved with FFT-based methods include: linear elasticity (Lebensohn, 2001; Brenner et al., 2009); linear viscosity (Lebensohn et al., 2005); thermoelasticity (Vinogradov and Milton, 2008; Anglin et al., 2014; Donegan and Rollett, 2015); rigid-viscoplasticity (Lebensohn, 2001; Lebensohn et al., 2008, 2009; Lee et al., 2011; Rollett et al., 2010); small-strain crystal plasticity elasto-viscoplasticity, i.e. CP-EVPFFT (Lebensohn et al., 2012; Grennerat et al., 2012; Suquet et al., 2012); large-strain elasto-viscoplasticity (Eisenlohr et al., 2013; Shanthraj et al., 2015; Kabel et al., 2016; Vidyasagar et al., 2018; Lucarini and Segurado, 2018); dilatational plasticity (Lebensohn et al., 2011,

2013); lower-order (Lucarini and Segurado, 2018) and higher-order strain-gradient plasticity (Lebensohn and Needleman, 2016); curvature-driven plasticity (Upadhyay et al., 2016); transformation plasticity (Richards et al., 2013; Otsuka et al., 2018); fatigue (Rovinelli et al., 2017a,b); and quasi-brittle damage (Li et al., 2012; Sharma et al., 2012). FFT-based methods were also applied to field dislocation mechanics (FDM) and field disclination mechanics (Brenner et al., 2014; Berbenni et al., 2014; Djaka et al., 2015; Berbenni et al., 2016; Djaka et al., 2017; Berbenni and Taupin, 2018), and discrete dislocation dynamics (DDD) problems (Bertin et al., 2015; Graham et al., 2016; Bertin and Capolungo, 2018), providing the efficiency needed for the implementation of these powerful and numerically-demanding formulations. The need for better numerical performance and stability of spectral approaches to avoid spurious oscillations of the local fields, known as the Gibbs phenomenon or aliasing, motivated the development of modified Green operators for the calculation of the displacement field and gradients of the latter in Fourier space (Willot and Pellegrini, 2008). For this, a successful numerical strategy (Berbenni et al., 2014; Lebensohn and Needleman, 2016) based on earlier works (Müller, 1996, 1998; Dreyer et al., 1999) consists in approximating derivatives in Cartesian space using finite differences (FD), and taking discrete Fourier transforms to these FD expressions. Among these FD-based schemes, a modified discrete Green operator based on centered FD on a rotated grid was proposed (Willot, 2015) and adopted in different subsequent FFT-based implementations (Djaka et al., 2017; Bertin and Capolungo, 2018; Lucarini and Segurado, 2018) given its good numerical performance. In their Galerkin discretization of the Lippmann-Schwinger equation, Brisard and Dormieux (2010) and Brisard and Dormieux (2012) proposed a numerical strategy based on a discrete Green operator which was adapted to a general variational framework based on the Hashin-Shtrikman energy principle. Another discrete Green operator was also recently proposed by Eloh et al. (2018) to numerically solve the Lippmann-

Schwinger equation for periodic heterogeneous composites with eigenstrains devoid of numerical oscillations. FFT-based predictions have been compared with other micromechanical solvers. For composites, Michel et al. (1999) carried out the first of these comparative studies with FE computations. Later on, CP-FEM and CP-FFT predictions for polycrystals deforming in different regimes were compared (Prakash and Lebensohn, 2009; Eisenlohr et al., 2013; Rovinelli et al., 2012), both in terms of microstructure and micromechanical field predictions. These comparisons were performed under several caveats, related to the different numerical strategies employed to solve the PDEs (weak form of equilibrium with FE vs. strong form with FFT-based methods), different discretization (mesh vs. grid), different boundary conditions (periodic unit cell required by FFT-based computations), and, in some cases, different kinematic assumptions and time integration schemes. Due to these differences, the corresponding predictions were not coincident point by point at local level, but the observed trends were, in general, qualitatively - and, in some cases, also quantitatively - similar.

All numerical implementations of the MFDM theory was carried out using FE. However, for polycrystalline materials, such a mechanics based formulation may take advantage of FFT-based methods, which were seen to be numerically efficient for elasto-static FDM (Berbenni et al., 2014; Djaka et al., 2017) and for the numerical spectral resolution of the dislocation density transport equation at constant applied GND velocity (Djaka et al., 2015). Therefore, the objective of the paper is to develop an EVPFFT-based method for MFDM in its reduced version, for describing size effects, slip constraints, flow stress due to both GNDs and SSDs and local GND dislocation density evolutions in the course of monotonous plastic deformation. Starting from the EVPFFT formulation developed by Lebensohn et al. (2012), it is based on five new pillars in comparison to the classic crystal plasticity

(CP-EVPFFT) formulation: (i) a new expression of the Jacobian for the augmented Lagrangian scheme inferred from MFDM, (ii) a numerical spectral resolution of the dislocation density transport equation involved in the MFDM theory, (iv) a hardening law accounting for GND density and a geometric mean free path due to GND, (iv) an interfacial jump condition on plastic distortion rate describing the conservation of Burgers vector content at material discontinuities between plastic channels and elastic second phase, and, (v) a spectral discrete method based on finite difference schemes to treat both lattice incompatibility and integral Lippmann-Schwinger equations.

The paper is organized as follows. In section 2, the constitutive equations of the Mesoscale Field Dislocation Mechanics (MFDM) are recalled. In this section, the jump condition on plastic distorsion rate across a material interface between elastic and plastic phases in laminate microstructures is also formulated. In section 3, the elasto-viscoplastic FFT-based numerical implementation for MFDM, named MFDM-EVPFFT, is presented. Section 4 is devoted to the numerical application of the MFDM-EVPFFT to periodic two-phase laminate microstructures with elastic and elasto-viscoplastic phases under shear loading. Plastic channel size effects will be reported for the MFDM-EVPFFT. Comparisons of the results regarding stresses, plastic distortions and dislocation densities between MFDM-EVPFFT and CP-EVPFFT will be discussed.

Notation

A bold symbol denotes a tensor or a vector. The symmetric part of tensor $\mathbf{A}$ is denoted $\mathbf{A}^{sym}$. Its skew-symmetric part is $\mathbf{A}^{skew}$ and its transpose is denoted by $\mathbf{A}^{t}$. The tensor $\mathbf{A} \cdot \mathbf{B}$, with rectangular Cartesian components $A_{ik}B_{kj}$, results from the dot

product of tensors $\mathbf{A}$ and $\mathbf{B}$, and $\mathbf{A} \otimes \mathbf{B}$ is their tensorial product, with components $A_{ij}B_{kl}$. The vector $\mathbf{A} \cdot \mathbf{V}$, with rectangular Cartesian components $A_{ij}V_j$, results from the dot product of tensor $\mathbf{A}$ and vector $\mathbf{V}$. The symbol " : " represents the trace inner product of the two second order tensors $\mathbf{A} : \mathbf{B} = A_{ij}B_{ij}$, in rectangular Cartesian components, or the product of a higher rank with a second rank tensor, e.g., $\mathbf{A} : \mathbf{B} = A_{ijkl}B_{kl}$. The cross product of a second rank tensor $\mathbf{A}$ and a vector $\mathbf{V}$, the **div** and **curl** operations for second rank tensors are defined row by row, in analogy with the vectorial case. For any base vector $\mathbf{e}_i$ of the reference frame:

$$(\mathbf{A} \times \mathbf{V})^t \cdot \mathbf{e}_i = (\mathbf{A}^t \cdot \mathbf{e}_i) \times \mathbf{V} \tag{1}$$
$$(\mathbf{div}\,\mathbf{A})^t \cdot \mathbf{e}_i = \mathbf{div}(\mathbf{A}^t \cdot \mathbf{e}_i) \tag{2}$$
$$(\mathbf{curl}\,\mathbf{A})^t \cdot \mathbf{e}_i = \mathbf{curl}(\mathbf{A}^t \cdot \mathbf{e}_i) \tag{3}$$

In rectangular Cartesian components:

$$(\mathbf{A} \times \mathbf{V})_{ij} = e_{jkl}A_{ik}V_l \tag{4}$$
$$(\mathbf{div}\mathbf{A})_i = A_{ij,j} \tag{5}$$
$$(\mathbf{curl}\,\mathbf{A})_{ij} = e_{jkl}A_{il,k} = -(\mathbf{grad}\,\mathbf{A} : \mathbf{X})_{ij} \tag{6}$$

where e_{jkl} is a component of the third rank alternating Levi-Civita tensor $\mathbf{X}$ and the spatial derivative with respect to a Cartesian coordinate is indicated by a comma followed by the component index. The notation $\widehat{\mathbf{A}}(\boldsymbol{\xi})$ will be used for the Fourier transform of $\mathbf{A}(\boldsymbol{x})$.

2 Theory: Mesoscale Field Dislocation Mechanics (MFDM)

2.1 Field equations of the Mesoscale Field Dislocation Mechanics (MFDM) theory (reduced version)

In a continuum mechanics setting, the displacement vector field $\mathbf{u}$ is defined continuously at any point of an elasto-viscoplastic body with volume V with external boundary S. At mesoscale, the total average distortion tensor, defined as the gradient of the average displacement $\mathbf{U} = \mathbf{grad\,u}$, is curl-free. In the presence of dislocation ensembles (Acharya, 2001; Roy and Acharya, 2005; Acharya and Roy, 2006), both the average plastic distortion $\mathbf{U}^p$, which results from dislocation motion, and the average elastic (or lattice) distortion $\mathbf{U}^e$ are incompatible fields. To solve the stress field $\boldsymbol{\sigma}$ and the displacement field $\mathbf{u}$, the following equations are solved in small deformation with standard traction/displacement boundary conditions on S_t and S_u respectively where $S = S_t U S_u$:

$$
\begin{aligned}
&\mathbf{div\,\boldsymbol{\sigma}} = 0 \\
&\boldsymbol{\sigma} = \mathbf{C} : \mathbf{U}^e \\
&\mathbf{U} = \mathbf{grad\,u} = \mathbf{U}^e + \mathbf{U}^p \\
&\boldsymbol{\sigma} \cdot \mathbf{n} = \overline{\mathbf{T}} \text{ on } S_t \\
&\mathbf{u} = \overline{\mathbf{u}} \text{ on } S_u
\end{aligned}
\tag{7}
$$

where $\mathbf{C}$ is the fourth order elastic stiffness tensor with classic minor and major symmetries such that $C_{ijkl} = C_{jikl} = C_{ijlk} = C_{klij}$.

In non local crystal plasticity theories based on continuum dislocation mechanics, dislocation ensembles can be categorized as Geometrically Necessary Dislocations (GNDs) and as Statistically Stored Dislocations (SSDs) (Ashby, 1970). This classification depends on the adopted resolution scale. Indeed, for a sufficiently fine scale

11

resolution (microscopic scale), all dislocations are polarized, i.e. GNDs. However at a fairly high resolution scale (mesoscopic scale), the presence of SSDs becomes more probable. SSDs accumulate within grains and only contribute to the overall plastic flow and not to long-range internal stresses, unlike GNDs which contribute to both. Therefore, considering a Burgers circuit at a microscopic scale, a single or an ensemble of polarized dislocations are represented by the dislocation density (or Nye) tensor $\boldsymbol{\alpha}$. Acharya (2001, 2003) used the dislocation density evolution equation to give a fundamental basis to the constitutive equation for the plastic strain rate. The expression of the plastic distortion rate $\dot{\mathbf{U}}^p$ due to dislocation motion as a function of the dislocation velocity $\mathbf{v}$ was given by Acharya (2011):

$$\dot{\mathbf{U}}^p = \boldsymbol{\alpha} \times \mathbf{v}. \tag{8}$$

At a mesoscopic scale represented by a larger Burgers circuit, the average value $\overline{\boldsymbol{\alpha}}$ of the dislocation density tensor $\boldsymbol{\alpha}$ can vanish. For example, this is the case when two densities of opposite signs and of the same nature statistically offset. However, their average plastic distortion rate $\overline{\boldsymbol{\alpha} \times \mathbf{v}}$ is non-vanishing and is not equal to $\overline{\boldsymbol{\alpha}} \times \overline{\mathbf{v}}$. It is due to the mobility of SSDs, represented by the mesoscale plastic strain rate denoted $\mathbf{L}^p$ where the averaging procedure was defined by Acharya and Roy (2006) as follows:

$$\mathbf{L}^p = \overline{(\boldsymbol{\alpha} - \overline{\boldsymbol{\alpha}}) \times \mathbf{v}} = \overline{\boldsymbol{\alpha} \times \mathbf{v}} - \overline{\boldsymbol{\alpha}} \times \overline{\mathbf{v}} \tag{9}$$

The mesoscale FDM theory (MFDM) is based on such considerations on the scale dependance. Here, a reduced version of the MFDM is considered (Roy et al., 2007), where all the fields of the latter are assumed to be as smooth as necessary. Hence, the average plastic distortion rate becomes:

$$\dot{\overline{\mathbf{U}}}^p = \overline{\boldsymbol{\alpha}} \times \overline{\mathbf{v}} + \mathbf{L}^p \tag{10}$$

From this equation, the plastic strain rate is deduced from the symmetric part of $\dot{\overline{\mathbf{U}}}^p$:

$$\dot{\overline{\varepsilon}}^p = \dot{\overline{\mathbf{U}}}^{p,sym} = (\overline{\boldsymbol{\alpha}} \times \overline{\mathbf{v}} + \mathbf{L}^p)^{sym} \tag{11}$$

The space-time evolution of the dislocation density tensor $\overline{\boldsymbol{\alpha}}$ is obtained from the conservation of dislocation flux and is prescribed as (Mura, 1963, 1964):

$$\dot{\overline{\boldsymbol{\alpha}}} = -\mathbf{curl}\, \dot{\overline{\mathbf{U}}}^p. \tag{12}$$

Constitutive specifications on the dislocation velocity $\overline{\mathbf{v}}$, and the slip distortion rate $\mathbf{L}^p$ are required for the MFDM theory. Therefore, $\mathbf{L}^p$ and $\overline{\mathbf{v}}$ are discussed using thermodynamic considerations following the theory introduced by Acharya and Roy (2006). For the sake of simplicity in the notation, the overbars denoting the space-time average quantity of a given tensor field or a vector field will be omitted in the remaining part of the paper. Therefore, eqs. 11 and 12 can be written in component forms:

$$\dot{\varepsilon}_{ij}^p = \frac{1}{2}\left(\dot{U}_{ij}^p + \dot{U}_{ji}^p\right) = \frac{1}{2}\left(L_{ij}^p + L_{ji}^p\right) + \frac{1}{2}\left((\alpha \times v)_{ij} + (\alpha \times v)_{ji}\right) \tag{13}$$

and:

$$\dot{\alpha}_{ij} = -\left(\alpha_{ij}v_k\right)_{,k} + \left(\alpha_{ik}v_j\right)_{,k} - e_{jkl}L_{il,k}^p \tag{14}$$

2.2 Constitutive equations

The constitutive equations for $\mathbf{L}^p$ and $\mathbf{v}$ are based on the rate of plastic work denoted D with the requirement to be positive and assuming pressure insensitive plasticity

(i.e. plastic incompressibility: $\dot{U}_{ii}^p = 0$). The expression of D was given by Acharya and Roy (2006):

$$D = \int_V \boldsymbol{\sigma} : \dot{\mathbf{U}}^p \, dV = \int_V \boldsymbol{\sigma} : \mathbf{L}^p \, dV + \int_V \boldsymbol{\sigma} : (\boldsymbol{\alpha} \times \mathbf{v}) \, dV \geq 0 \qquad (15)$$

The last expression can be simplified using the third order Levi-Civita tensor $\mathbf{X}$ (see section 1) such that finally eq. 15 reads:

$$D = \int_V \boldsymbol{\sigma} : \mathbf{L}^p \, dV + \int_V \mathbf{F}^\alpha \cdot \mathbf{v} \, dV \geq 0 \qquad (16)$$

where $\mathbf{F}^\alpha$ is the Peach-Koehler driving force for GND motion which is the thermodynamic conjugate of $\mathbf{v}$. The GND velocity vector $\mathbf{v}$ depends on the stress field $\boldsymbol{\sigma}$. In component form, the Peach-Koehler thermodynamic force $\mathbf{F}^\alpha$ is defined as:

$$F_l^\alpha = e_{ikl}\sigma_{ij}\alpha_{jk} \qquad (17)$$

In crystal plasticity, the plastic distortion rate tensor $\mathbf{L}^p$ due to slip inferred from SSDs is defined as:

$$\mathbf{L}^p = \sum_{s=1}^N \dot{\gamma}^s \mathbf{b}^s \otimes \mathbf{n}^s = \sum_{s=1}^N \dot{\gamma}^s \mathbf{m}^s, \qquad (18)$$

where N, $\dot{\gamma}^s$ and $\mathbf{m}^s$ are the number of slip systems, the slip rate and the crystallographic orientation tensor such that $\mathbf{m}^s = \mathbf{b}^s \otimes \mathbf{n}^s$. For each slip system s, the unit vector $\mathbf{b}^s$ denotes the slip direction and $\mathbf{n}^s$ the slip plane unit normal. Therefore, the expression of $\mathbf{L}^p$ is similar to the classic crystal plasticity formulations as the one used in the FFT-based model for elasto-viscoplastic polycrystals (Lebensohn et al., 2012). Let us note that the expression of $\mathbf{L}^p$ is based on a crystal plasticity formulation as in Puri et al. (2011), which is different from the works of Acharya and Roy (2006), Roy et al. (2007) and Puri et al. (2009) who considered a J_2 isotropic plastic flow theory. Plastic flow incompressibility is considered from the fact that $\mathbf{L}^p$
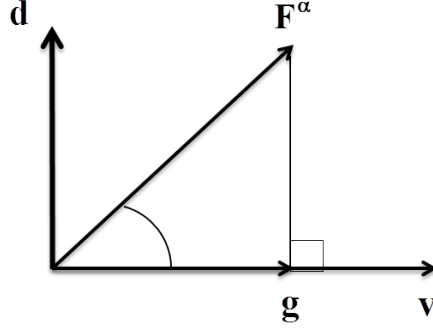
14

Figure 1. Vectorial representation of the thermodynamic driving force $\mathbf{F}^\alpha$ for GND motion. Geometric definitions of the glide force $\mathbf{g}$ such that $\mathbf{g}$ is parallel to the average GND velocity vector $\mathbf{v}$ and the dilatant vector $\mathbf{d}$ is defined such that $\mathbf{d}$ is orthogonal to $\mathbf{v}$.

and $\boldsymbol{\alpha} \times \mathbf{v}$ are traceless. Therefore, this property yields:

$$L_{ii}^p = 0 \quad \text{from} \quad m_{ii}^s = 0 \quad \text{for all } s \tag{19}$$

and:

$$e_{ikl}\alpha_{ik}v_l = 0 \quad \implies \quad d_l v_l = 0 \tag{20}$$

with:

$$d_l = e_{mnl}\alpha_{mn} \tag{21}$$

where $\mathbf{d}$ is the dilatant direction such that $\mathbf{d} \perp \mathbf{v}$ as defined in Fig. 1.

To fulfill these thermodynamics requirements, the GND velocity $\mathbf{v}$ is prescribed as follows:

$$\mathbf{v} = \frac{\mathbf{g}}{|\mathbf{g}|}\bar{v} \quad \text{with} \quad \bar{v} \geq 0, \tag{22}$$

where $\mathbf{g}$ and $\bar{v}$ are the glide force parallel to $\mathbf{v}$ and the magnitude of $\mathbf{v}$ respectively. The glide force is defined from geometry using Fig. 1:

$$\mathbf{g} = \mathbf{F}^\alpha - \left(\mathbf{F}^\alpha \cdot \frac{\mathbf{d}}{|\mathbf{d}|}\right)\frac{\mathbf{d}}{|\mathbf{d}|}, \tag{23}$$

After further derivations, the glide force $\mathbf{g}$ can be explicitly written as (Acharya and Roy, 2006):

$$\mathbf{g} = \mathbf{b} - \left(\mathbf{b} \cdot \frac{\mathbf{a}}{|\mathbf{a}|}\right)\frac{\mathbf{a}}{|\mathbf{a}|} \tag{24}$$

15

where **b** and **a** are given in component form:

$$b_r = e_{ikr}\alpha_{jk}S_{ij}$$
$$a_r = e_{ikr}\alpha_{ik}\left(\frac{1}{3}\sigma_{kk}\right) = d_r\left(\frac{1}{3}\sigma_{kk}\right) \tag{25}$$

where $S_{ij} = \sigma_{ij} - \frac{1}{3}\sigma_{kk}\delta_{ij}$ is the deviatoric stress tensor.

Using eq. 22 together with eq. 23, the component form of **g** is given by:

$$g_r = e_{ikr}\alpha_{jk}S_{ij} - e_{ikr}\alpha_{ik}\frac{S_{mn}\alpha_{np}(\alpha_{mp} - \alpha_{pm})}{\alpha_{ij}(\alpha_{ij} - \alpha_{ji})}, \tag{26}$$

The constitutive equations adopted for $\bar{v}$ and $\dot{\gamma}^s$ are based on the Orowan law for GND and SSD mobile dislocations, respectively and an empirical Taylor-Bailey-Hirsch relationship for the shear strength of the material. Here, a mechanistic formulation for $\bar{v}$ similar to Puri et al. (2010, 2011) is adopted:

$$\bar{v} = \frac{\eta^2 b}{N}\left(\frac{\mu}{\tau_c}\right)^2 \sum_{s=1}^{N} |\dot{\gamma}^s| \tag{27}$$

where η is a material constant close to $1/3$ (Ashby, 1970), b is the magnitude of the Burgers vector, τ_c is the shear strength and μ is the isotropic elastic shear modulus of the material. The slip rate $\dot{\gamma}^s$ is defined with a classic viscoplastic flow rule as a power law:

$$\dot{\gamma}^s = \dot{\gamma}^0 \left(\frac{|\tau^s|}{\tau_c}\right)^{1/m} sgn(\tau^s) \tag{28}$$

where m represents the rate sensitivity of the material, $\tau^s = \mathbf{m}^s : \boldsymbol{\sigma}$ is the resolved shear stress, $\dot{\gamma}^0$ is the reference slip rate and τ_c is considered identical for all slip systems.

In contrast with Puri et al. (2010, 2011), no intra-crystalline phenomenological back-stress evolution is considered since the applications (see section 4) will not be con-

cerned by cyclic plasticity. The cumulated slip rate on all slip systems due to both
GNDs and SSDs is given by:

$$\dot{\Gamma} = |\boldsymbol{\alpha} \times \mathbf{v}| + \sum_{s=1}^{N} |\dot{\gamma}^s| \tag{29}$$

The evolution law for the shear strength τ_c follows the same hypotheses as the strain-
hardening model developed by Puri et al. (2010, 2011), which is an extension of the
earlier models derived by Mecking and Kocks (1981) and Acharya and Beaudoin
(2000):

$$\dot{\tau}_c = \theta_0 \frac{\tau_s - \tau_c}{\tau_s - \tau_0} \dot{\Gamma} + k_0 \frac{\eta^2 \mu^2 \, b}{2 \, (\tau_c - \tau_0)} \left(\sum_{s=1}^{N} |\boldsymbol{\alpha} \cdot \mathbf{n}^s| \, |\dot{\gamma}^s| + \sum_{s=1}^{N} |\boldsymbol{\alpha} \cdot \mathbf{n}^s| \, |\boldsymbol{\alpha} \times \mathbf{v}| \right) \tag{30}$$

where τ_0 is the yield strength due to lattice friction (this value is relatively low
for face-centered cubic (FCC) metals), τ_s is the saturation stress, θ_0 is the stage II
hardening rate for FCC metals. Furthermore, the material parameter k_0 is related
to a geometric mean free path due to GND forest on slip system s (Acharya and
Beaudoin, 2000):

$$L_g = \frac{1}{k_0 \, |\boldsymbol{\alpha} \cdot \mathbf{n}^s|} \tag{31}$$

In the next simulations reported in section 4, a value for k_0 close to one fitted by
Acharya and Beaudoin (2000) for FCC metals will be used. For comparison, in the
case of a model based on conventional crystal plasticity (no GND, i.e. $\boldsymbol{\alpha} = \mathbf{0}$), eq.
30 reduces to classic Voce-type law (Kocks, 1976):

$$\dot{\tau}_c = \theta_0 \frac{\tau_s - \tau_c}{\tau_s - \tau_0} \dot{\Gamma} \tag{32}$$

with:

$$\dot{\Gamma} = \sum_{s=1}^{N} |\dot{\gamma}^s| \tag{33}$$

17

instead of eq. 29.

2.3 Explicit dislocation density transport equation

The numerical treatment for solving the space-time evolution of the dislocation density tensor (see eq. 12) was reported by Varadhan et al. (2006) and Djaka et al. (2017) in the framework of Field Dislocation Mechanics (FDM). In these contributions, an explicit forward Euler scheme was derived to numerically solve this equation starting from an implicit backward Euler scheme together with a Taylor expansion at first order of $\alpha_{ij}^{t+\triangle t}$ where $\triangle t$ is the time step. In the case of MFDM, eq. 12 together with eq. 10 can be first written in component form using an implicit backward Euler scheme:

$$\alpha_{ij}^{t+\triangle t} = \alpha_{ij}^t - \triangle t \, \left((\alpha_{ij}v_k)^{t+\triangle t} - (\alpha_{ik}v_j)^{t+\triangle t} + e_{jkl} \, (L_{il}^p)^{t+\triangle t} \right)_{,k} \tag{34}$$

and using $\alpha_{ij}^{t+\triangle t} = \alpha_{ij}^t + \triangle t \, \dot{\alpha}_{ij}^t + 0\left(\triangle t^2\right)$ and $(L_{ij}{}^p)^{t+\triangle t} = (L_{ij}{}^p)^t + \triangle t \, (\dot{L_{ij}{}^p})^t + 0\left(\triangle t^2\right)$. Then, the first order Taylor approximation of $\alpha_{ij}{}^{t+\triangle t}$ and $(L_{ij}{}^p)^{t+\triangle t}$ in eq. 34 leads to the explicit forward explicit scheme (Varadhan et al., 2006):

$$\alpha_{ij}^{t+\triangle t} = \alpha_{ij}^t - \triangle t \, \left((\alpha_{ij}v_k)^t - (\alpha_{ik}v_j)^t + e_{jkl} \, (L_{il}^p)^t \right)_{,k} \tag{35}$$

This equation will be solved later in the Fourier space (see section 3) with an efficient numerical spectral approach that uses an exponential low-pass filter (Djaka et al., 2015).
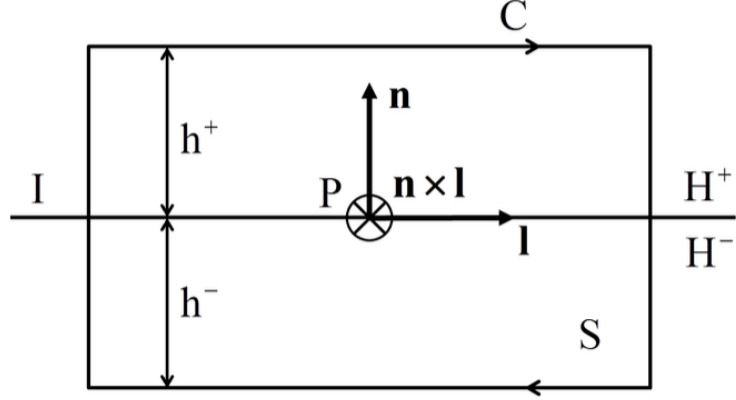
18

Figure 2. Schematic figure of a material interface I between two different media $+$ and $-$ with $\mathbf{n}$ is the unit outward normal vector to the interface directed from medium $-$ to medium $+$.

2.4   Jump condition on plastic distorsion rate across a material interface

In contrast with conventional elasto-viscoplastic crystal plasticity theories, the evolution equations for MFDM impose a jump condition on plastic distorsion rate across a material interface (Fig. 2). This jump condition allows modeling specific requirements regarding the interaction of dislocations with impenetrable or penetrable interfaces. Following Acharya (2007), the general condition for a fixed (i.e. non moving) interface writes:

$$[\dot{\mathbf{U}}^p] \times \mathbf{n} = [\boldsymbol{\alpha} \times \mathbf{v} + \mathbf{L}^\mathbf{p}] \times \mathbf{n} = \mathbf{0} \tag{36}$$

where $\mathbf{n}$ is the unit outward normal vector to the interface I (Fig. 2) and $[\dot{\mathbf{U}}^p] = \dot{\mathbf{U}}^{p(+)} - \dot{\mathbf{U}}^{p(-)}$ is the jump of $\dot{\mathbf{U}}^p$ between both media $+$ and $-$.

Here, two-phase laminate microstructures are considered (see Fig. 3 in section 4), which are constituted of purely elastic inclusions (elastic second phase, blue colored) and plastic channels (elasto-viscoplastic phase, red colored). Therefore, $\dot{\mathbf{U}}^p$ is non zero only in the plastic channels, i.e. the elasto-viscoplastic phase. In the case

19

of impenetrable grain/phase boundaries to dislocations, which corresponds to the modeling of completely constrained plastic flow at the interface, this condition yields according to Puri et al. (2011):

$$\dot{\mathbf{U}}^p \times \mathbf{n} = 0 \tag{37}$$

A sufficient condition to satisfy eq. 37 is that:

$$\mathbf{L^P} \times \mathbf{n} = 0 \text{ and } \boldsymbol{\alpha} \times \mathbf{v} \times \mathbf{n} = 0 \tag{38}$$

with $L_{ii}^p = 0$ and $e_{ikl}\alpha_{ik}v_l = 0$ due to plastic incompressibility from eqs. 19 and 20, respectively. Furthermore, Acharya (2007) showed that $\boldsymbol{\alpha} \times \mathbf{v} \times \mathbf{n}$ writes:

$$\boldsymbol{\alpha} \times \mathbf{v} \times \mathbf{n} = -\boldsymbol{\alpha}^{tan}\left(\mathbf{v} \cdot \mathbf{n}\right) + \boldsymbol{\alpha} \cdot \mathbf{n} \otimes \mathbf{v}^{tan} \tag{39}$$

where $\alpha_{ij}{}^{tan} = \alpha_{ij} - (\alpha_{ik}n_k)n_j$ and $v_i{}^{tan} = v_i - (v_j n_j)n_i$.

Using the Cartesian coordinates chosen in Fig. 3, the unit vectors along the y-, z-, x- directions are defined as $\mathbf{e}_2 = \mathbf{n}$, $\mathbf{e}_3 = \mathbf{l}$ et $\mathbf{e}_1 = \mathbf{n} \times \mathbf{l}$, respectively. Therefore, the first equation of eq. 38 yields the interfacial condition on $\mathbf{L^P}$:

$$\mathbf{L^P} = \begin{pmatrix} 0 & L_{12}^p & 0 \\ 0 & 0 & 0 \\ 0 & L_{32}^p & 0 \end{pmatrix} \tag{40}$$

which corresponds to a single slip situation with slip plane parallel to the interface and non zero slip rate ($\dot{\gamma}^s \neq 0$). Such condition was also discussed by Gurtin and Needleman (2005) who named this condition as a *microhard condition* which is different from the so-called *hard slip condition* ($\dot{\gamma}^s = 0$). Using eq. 39, the second

equation of eq. 38 yields:

$$\boldsymbol{\alpha} \times \mathbf{v} \times \mathbf{e}_2 = -\boldsymbol{\alpha}^{tan} \left(\mathbf{v} \cdot \mathbf{e}_2\right) + \boldsymbol{\alpha} \cdot \mathbf{e}_2 \otimes \mathbf{v}^{tan} = 0 \tag{41}$$

A physical sufficient condition to satisfy $\boldsymbol{\alpha} \times \mathbf{v} \times \mathbf{n} = 0$ is to assume that both $\mathbf{v} \cdot \mathbf{e}_2 = v_2 = 0$ and $\boldsymbol{\alpha} \cdot \mathbf{e}_2 = \alpha_{i2} = 0$. Furthermore, plastic incompressibility (eq. 20) leads to $\alpha_{23} = \alpha_{32} = 0$ and $\alpha_{21} = \alpha_{12} = 0$. Therefore, the interfacial jump condition on GND density tensor $\boldsymbol{\alpha}$ writes:

$$\begin{cases} \alpha_{12} = \alpha_{32} = \alpha_{23} = \alpha_{21} = \alpha_{22} = 0 \quad \text{such that:} \\ \\ \boldsymbol{\alpha} = \begin{pmatrix} \alpha_{11} & 0 & \alpha_{13} \\ 0 & 0 & 0 \\ \alpha_{31} & 0 & \alpha_{33} \end{pmatrix} \end{cases} . \tag{42}$$

According to these assumptions, both eqs. 40 and 42 constitute interfacial conditions which produce a change of plastic distortion rate due to impenetrable interfaces that is not specified by the above constitutive equations reported in section 2.2.

3   Elasto-viscoplastic FFT-based numerical implementation for MFDM: MFDM-EVPFFT formulation

3.1   *Elasto-viscoplastic FFT formulation with augmented Lagrangian scheme*

Here, an elasto-viscoplastic crystal plasticity formulation is adopted in a small deformation setting. Using a backward Euler implicit time discretization and the generalized Hooke's law, the expression of the stress at $t + \triangle t$ is given by:

$$\boldsymbol{\sigma}^{t+\triangle t} = \mathbf{C} : \boldsymbol{\varepsilon}^{e,t+\triangle t} = \mathbf{C} : \left(\boldsymbol{\varepsilon}^{t+\triangle t} - \boldsymbol{\varepsilon}^{p,t} - \dot{\boldsymbol{\varepsilon}}^{p,t+\triangle t}(\boldsymbol{\sigma}^{t+\triangle t})\triangle t \right), \qquad (43)$$

where, $\boldsymbol{\sigma}$ is the Cauchy stress tensor, $\mathbf{C}$ is the elastic stiffness tensor, $\boldsymbol{\varepsilon}$, $\boldsymbol{\varepsilon}^e$ and $\boldsymbol{\varepsilon}^p$ are the total, elastic and plastic strain tensors, and $\dot{\boldsymbol{\varepsilon}}^p$ is the plastic strain rate which represents the symmetric part of the plastic distortion rate defined in Eq. 13. In what follows, the supra-indices $t + \triangle t$ are omitted for sake of simplicity, and only the fields corresponding to the previous time step t will be explicitly indicated. Therefore, the constitutive equation and its inverse read in component forms (Lebensohn et al., 2012):

$$\begin{aligned}
\sigma_{ij} &= C_{ijkl} \left(\varepsilon_{kl} - \varepsilon_{kl}^{p,t} - \dot{\varepsilon}_{kl}^{p}(\boldsymbol{\sigma})\triangle t \right) \\
\varepsilon_{ij} &= C_{ijkl}^{-1}\sigma_{kl} + \varepsilon_{ij}^{p,t} + \dot{\varepsilon}_{ij}^{p}(\boldsymbol{\sigma})\triangle t
\end{aligned} \qquad (44)$$

For periodic heterogeneous media, the balance of linear momentum without body forces and inertia forces (see first equation in eq. 7) can be solved using the Green's function technique (Mura, 1987) through an integral Lippmann-Schwinger equation. Assuming a homogeneous reference medium with linear elastic moduli $\mathbf{C}^0$, such that $\mathbf{C} = \mathbf{C}^0 + \delta\mathbf{C}$, the stress equilibrium equation yields, in component form:

$$C_{ijkl}^0 u_{k,lj} + \tau_{ij,j} = 0 \qquad (45)$$

In this equation, $\mathbf{u}$ represents the displacement vector and $\boldsymbol{\tau}$ represents the stress polarization tensor field due to heterogeneities and defined in component form as follows:

$$\tau_{ij} = \sigma_{ij} - C_{ijkl}^0 u_{k,l} = \sigma_{ij} - C_{ijkl}^0 \varepsilon_{kl} \qquad (46)$$

Since $\boldsymbol{\tau}$ contains the unknown total strain field $\boldsymbol{\varepsilon}$, eq. 45 is solved through an integral Lippmann-Schwinger equation for the unknown strain field $\boldsymbol{\varepsilon}$:

$$\varepsilon_{ij}(\mathbf{x}) = \langle \varepsilon_{ij} \rangle - \int_V \Gamma_{ijkl}^0(\mathbf{x} - \mathbf{x}')\tau_{kl}(\mathbf{x}')dV' \qquad (47)$$

where $\langle \varepsilon \rangle$ represents the average value of the ε in V and Γ^0_{ijkl} is the modified Green tensor associated with the homogeneous elastic moduli $\mathbf{C}^0$:

$$\Gamma^0_{ijkl}(\mathbf{x} - \mathbf{x}') = -\frac{1}{4} \left(G_{ik,jl}(\mathbf{x} - \mathbf{x}') + G_{jk,il}(\mathbf{x} - \mathbf{x}') + G_{il,kj}(\mathbf{x} - \mathbf{x}') + G_{jl,ki}(\mathbf{x} - \mathbf{x}') \right)$$

(48)

where $\mathbf{G}(\mathbf{x} - \mathbf{x}')$ is the classic elastic Green tensor associated with $\mathbf{C}^0$. In the following, eq. 47 together with eq. 44 will be solved using a computationally efficient scheme based on Fast Fourier Transform (FFT) and augmented Lagrangian introduced by Michel et al. (2001).

In the Fourier space, let $\boldsymbol{\xi}$ be the Fourier vector of magnitude $\xi = \sqrt{\boldsymbol{\xi} \cdot \boldsymbol{\xi}}$ and components ξ_i in a general three-dimensional Cartesian coordinate system setting. The complex imaginary number is denoted i and defined as $i = \sqrt{-1}$. Let $\widehat{\varepsilon}(\boldsymbol{\xi})$ and $\widehat{\boldsymbol{\Gamma}}^0(\boldsymbol{\xi})$ be, respectively, the continuous Fourier transform of $\varepsilon(\boldsymbol{x})$ and $\boldsymbol{\Gamma}^0(\mathbf{x})$. The Fourier transform of the integral Lippmann-Schwinger equation (eq. 47) yields:

$$\widehat{\varepsilon}(\boldsymbol{\xi}) = -\widehat{\boldsymbol{\Gamma}}^0(\boldsymbol{\xi}) : \widehat{\boldsymbol{\tau}}(\boldsymbol{\xi}) \ \forall \boldsymbol{\xi} \neq \mathbf{0}$$
$$\widehat{\varepsilon}(\mathbf{0}) = \langle \boldsymbol{\varepsilon} \rangle$$

(49)

The Fourier Transform of the modified Green operator $\boldsymbol{\Gamma}^0$, is given by the following formula:

$$\widehat{\Gamma}^0_{ijkl}(\boldsymbol{\xi}) = \frac{1}{4} \left(\widehat{G}_{ik}(\boldsymbol{\xi})\xi_l\xi_j + \widehat{G}_{jk}(\boldsymbol{\xi})\xi_l\xi_i + \widehat{G}_{il}(\boldsymbol{\xi})\xi_k\xi_j + \widehat{G}_{jl}(\boldsymbol{\xi})\xi_k\xi_i \right)$$

(50)

with:

$$\begin{cases} \widehat{G_{ij}}(\boldsymbol{\xi}) = \dfrac{N_{ij}(\boldsymbol{\xi})}{D(\boldsymbol{\xi})} & \forall \boldsymbol{\xi} \neq 0 \\[3mm] \widehat{G_{ij}}(\mathbf{0}) = 0 \end{cases}$$

(51)

where $N_{ij}(\boldsymbol{\xi})$ denotes the rectangular components of the cofactor matrix related to the acoustic tensor $K_{ij} = C^o_{ijkl}\xi_k\xi_l$ and $D(\boldsymbol{\xi})$ is the determinant of K_{ij}. Due to the symmetry properties of C^o_{ijkl}, $N_{ij}(\boldsymbol{\xi})$ satisfies: $N_{ij}(\boldsymbol{\xi}) = N_{ji}(\boldsymbol{\xi})$, therefore $\widehat{G_{ij}} = \widehat{G_{ji}}$

and $\widehat{\Gamma}^0_{ijkl} = \widehat{\Gamma}^0_{jikl} = \widehat{\Gamma}^0_{ijlk} = \widehat{\Gamma}^0_{klij}$. For isotropic elasticity using the two Lamé constants, the expression of $\widehat{\Gamma}^0_{ijkl}$ was given in Moulinec and Suquet (1994, 1998).

Let us assume now that $\lambda^{(n)}_{ij}$ and $e^{(n)}_{ij}$ are, respectively, the auxiliary guess stress and strain fields at iteration (n). The stress polarization tensor (Eq. 46) becomes (Michel et al., 2001):

$$\tau^{(n)}_{ij} = \lambda^{(n)}_{ij} - C^0_{ijkl} e^{(n)}_{kl} \tag{52}$$

The new guess for the strain field is given in Fourier space as:

$$\widehat{e}^{(n+1)}_{ij}(\boldsymbol{\xi}) = -\widehat{\Gamma}^0_{ijkl}(\boldsymbol{\xi})\widehat{\tau}^{(n)}_{kl}(\boldsymbol{\xi}) \ \forall \boldsymbol{\xi} \neq \mathbf{0}$$
$$\widehat{e}^{(n+1)}_{ij}(\mathbf{0}) = \langle \boldsymbol{\varepsilon}^n \rangle \tag{53}$$

An alternative fixed-point expression, which requires computing the Fourier transform of the stress field instead of that of the polarization field was reported in Michel et al. (2001):

$$\widehat{e}^{(n+1)}_{ij}(\boldsymbol{\xi}) = \widehat{e}^{(n)}_{ij}(\boldsymbol{\xi}) - \widehat{\Gamma}^0_{ijkl}(\boldsymbol{\xi})\widehat{\lambda}^{(n)}_{kl}(\boldsymbol{\xi}) \ \forall \boldsymbol{\xi} \neq \mathbf{0}$$
$$\widehat{e}^{(n+1)}_{ij}(\mathbf{0}) = \langle \boldsymbol{\varepsilon}^n \rangle \tag{54}$$

Once $e^{(n+1)}_{ij} = \mathrm{FT}^{-1}(\widehat{e}^{(n+1)}_{ij}(\boldsymbol{\xi}))$ is obtained in the real space by using the inverse Fourier transform (FT^{-1}), the nullification of the residual $\mathbf{R}$, which depends on the stress and strain tensors $\boldsymbol{\sigma}^{(n+1)}$ and $\boldsymbol{\varepsilon}^{(n+1)}$, is solved:

$$R_{ij}(\boldsymbol{\sigma}^{(n+1)}) = \sigma^{(n+1)}_{ij} + C^0_{ijmn}\varepsilon^{(n+1)}_{mn}(\boldsymbol{\sigma}^{(n+1)}) - \lambda^{(n)}_{ij} - C^0_{ijmn}e^{(n+1)}_{mn} = 0 \tag{55}$$

This nonlinear equation was solved by Lebensohn et al. (2012) using a Newton-Raphson-type scheme. The $(p+1)$-guess for the stress field $\boldsymbol{\sigma}^{(n+1)}_{ij}$ is given by:

$$\sigma_{ij}^{(n+1,p+1)} = \sigma_{ij}^{(n+1,p)} - \left(\left(\frac{\partial R_{ij}}{\partial \sigma_{mn}} \right)_{\boldsymbol{\sigma}^{(n+1,p)}} \right)^{-1} R_{mn} \left(\boldsymbol{\sigma}^{(n+1,p)} \right) \tag{56}$$

Using the constitutive specifications (eq. 44) and eq. 55, the Jacobian in the above expression reads:

$$\left(\frac{\partial R_{ij}}{\partial \sigma_{mn}} \right)_{\boldsymbol{\sigma}^{(n+1,p)}} = \delta_{im}\delta_{jn} + C_{ijkl}^0 C_{klmn}^{-1} + \triangle t\, C_{ijkl}^0 \left(\frac{\partial \dot{\varepsilon}_{kl}^p}{\partial \sigma_{mn}} \right)_{\boldsymbol{\sigma}^{(n+1,p)}} \tag{57}$$

Once the convergence is achieved on $\boldsymbol{\sigma}^{(n+1)}$ and $\boldsymbol{\varepsilon}^{(n+1)}$, the new guess for the auxiliary stress field $\boldsymbol{\lambda}$ is given by using the Uzawa descent algorithm:

$$\lambda_{ij}^{(n+1)} = \lambda_{ij}^{(n)} + C_{ijkl}^0 \left(e_{kl}^{(n+1)} - \varepsilon_{kl}^{(n+1)} \right) \tag{58}$$

and the algorithm is stopped when the normalized average differences between the stress fields $\boldsymbol{\sigma}$ and $\boldsymbol{\lambda}$, and the strain fields $\boldsymbol{\varepsilon}$ and $\mathbf{e}$, are smaller than a given threshold error (typically 10^{-5}). This condition implies the fulfillment of both stress equilibrium and strain compatibility up to sufficient accuracy.

In the algorithm described above, an overall macroscopic strain $\mathbf{E} = \langle \boldsymbol{\varepsilon}^n \rangle$ is applied to the periodic unit cell V in the form of:

$$E_{ij} = E_{ij}^t + \dot{E}_{ij}\triangle t \tag{59}$$

In cases of mixed boundary conditions with imposed macroscopic strain rate $\dot{E}_{ij}$ and stress Σ_{ij}, the $(n+1)$-guess of the macroscopic strain $E_{ij}^{(n+1)}$ is (Michel et al., 2001; Lebensohn et al., 2012):

$$E_{ij}^{(n+1)} = E_{ij}^{(n)} + C_{ijkl}^{0-1}\omega^{[kl]} \left(\Sigma_{kl} - \langle \lambda_{kl}^{(n+1)} \rangle \right) \tag{60}$$

where $\omega^{[kl]} = 1$ if component Σ_{kl} is imposed and zero otherwise.

3.2 New expression of the Jacobian for augmented Lagrangian scheme inferred from MFDM

In eq. 57, the new expression of $\partial\dot{\varepsilon}^p_{kl}/\partial\sigma_{mn}$ considering the constitutive equations of the MFDM theory yields:

$$\left(\frac{\partial\dot{\varepsilon}^p_{kl}}{\partial\sigma_{mn}}\right)_{\boldsymbol{\sigma}^{(n+1,p)}} = \frac{1}{2}\left(\frac{\partial L^p_{kl}}{\partial\sigma_{mn}} + \frac{\partial L^p_{lk}}{\partial\sigma_{mn}}\right)_{\boldsymbol{\sigma}^{(n+1,p)}} + \frac{1}{2}\left(\frac{\partial(\alpha\times v)_{kl}}{\partial\sigma_{mn}} + \frac{\partial(\alpha\times v)_{lk}}{\partial\sigma_{mn}}\right)_{\boldsymbol{\sigma}^{(n+1,p)}}$$

(61)

According to eqs. 18 and 28, an approximation expression of $\partial L^p_{kl}/\partial\sigma_{mn}$ is given by:

$$\left(\frac{\partial L^p_{kl}}{\partial\sigma_{mn}}\right)_{\boldsymbol{\sigma}^{(n+1,p)}} \simeq n\dot{\gamma}^0\sum_{s=1}^{N} m^s_{kl}P^s_{mn}\frac{|P^s_{mn}\sigma_{mn}|^{n-1}}{(\tau_c)^n}$$

(62)

where $\mathbf{P}^s = (\mathbf{m}^s)^{sym}$. In eq. 62, the approximation lies in the fact that the derivatives $\partial\tau_c/\partial\boldsymbol{\sigma}$ and $\partial\mathbf{P}^s/\partial\boldsymbol{\sigma}$ are neglected.

The determination of the expression of $\partial(\alpha\times v)_{kl}/\partial\sigma_{mn}$ is new compared to the standard EVPFFT formulation:

$$\left(\frac{\partial(\alpha\times v)_{kl}}{\partial\sigma_{mn}}\right)_{\boldsymbol{\sigma}^{(n+1,p)}} = e_{lqr}\alpha_{kq}\left(\frac{\partial v_r}{\partial\sigma_{mn}}\right)_{\boldsymbol{\sigma}^{(n+1,p)}}$$

(63)

Eq. 63 can be written more explicitly by considering eqs. 22 and 23 as:

$$\left(\frac{\partial(\alpha\times v)_{kl}}{\partial\sigma_{mn}}\right)_{\boldsymbol{\sigma}^{(n+1,p)}} = e_{lqr}\alpha_{kq}\left(\frac{\partial(g_r/|\mathbf{g}|)}{\partial\sigma_{mn}}\bar{v} + \frac{g_r}{|\mathbf{g}|}\frac{\partial\bar{v}}{\partial\sigma_{mn}}\right)_{\boldsymbol{\sigma}^{(n+1,p)}}$$

(64)

with:

$$\frac{\partial(g_r/|\mathbf{g}|)}{\partial\sigma_{mn}} = \left(\frac{\delta_{rs}|\mathbf{g}|^2 - g_r g_s}{|\mathbf{g}|^3}\right)\left(e_{oks}\alpha_{qk} - e_{iks}\alpha_{ik}\frac{\alpha_{qp}(\alpha_{op}-\alpha_{po})}{\alpha_{ij}(\alpha_{ij}-\alpha_{ji})}\right)$$
$$\left(\delta_{om}\delta_{qn} - \frac{1}{3}\delta_{mn}\delta_{oq}\right)$$

(65)

and using eq. 27 with the same approximation as in eq. 62:

$$\left(\frac{\partial\bar{v}}{\partial\sigma_{mn}}\right)_{\boldsymbol{\sigma}^{(n+1,p)}} \simeq n\dot{\gamma}^0\frac{\eta^2\,b}{N}\left(\frac{\mu}{\tau_c}\right)^2\sum_{s=1}^{N}P^s_{mn}\frac{|P^s_{mn}\sigma_{mn}|^{n-1}}{(\tau_c)^n}$$

(66)

3.3   Spectral resolution of the dislocation density transport equation

Let $\widehat{\boldsymbol{\alpha}}(\boldsymbol{\xi})$ be the continuous Fourier transform of $\boldsymbol{\alpha}(\boldsymbol{x})$. Therefore the Fourier transform of Eq. 35 is given by:

$$\widehat{\alpha}_{ij}^{t+\triangle t} = \widehat{\alpha}_{ij}^{t} - \triangle t\,\mathrm{i}\,\xi_k\,\left(\widehat{(\alpha_{ij}v_k)}^{t} - \widehat{(\alpha_{ik}v_j)}^{t} + e_{jkl}\widehat{(L_{il}^{p})}^{t}\right) \tag{67}$$

As pointed out in Djaka et al. (2015), the resolution of Eq. 67 in the Fourier space without the source term $e_{jkl}\widehat{(L_{il}^{p})}^{t}$ leads to non accurate and unstable solution due to the occurrence of high-frequency Gibbs oscillations inherent to the Fourier method and to the fast-growing numerical instabilities resulting from its hyperbolic nature. Therefore, an exponential second order spectral low-pass filter was used to stabilize the numerical approximation by eliminating high frequencies leading to spurious oscillations. The exponential filter is defined as function of frequencies η as:

$$\kappa\left(\eta\right) = \exp\left(-\beta\left(\eta\right)^{2p}\right), \tag{68}$$

According to Gottlieb and Hesthaven (2001), the damping parameter β is defined as $\beta = -\log\varepsilon_M$, where ε_M is low value parameter that was optimized by Djaka et al. (2015). Both parameters ϵ_M and p will be specified in section 4.1 for the present application. Applying the exponential filter to eq. 67 yields:

$$\widehat{\alpha}_{ij}^{t+\triangle t} = \kappa\left(\eta\right)\left(\widehat{\alpha}_{ij}^{t} - \triangle t\,\mathrm{i}\,\xi_k\,\left(\widehat{(\alpha_{ij}v_k)}^{t} - \widehat{(\alpha_{ik}v_j)}^{t}\right)\right) - \triangle t\,\mathrm{i}\,\xi_k\,e_{jkl}\widehat{(L_{il}^{p})}^{t} \tag{69}$$

To fix the time step $\triangle t$ in eq. 69 to satisfy stability requirements for numerically solving the dislocation density transport equation, a user-specified fraction denoted c of Courant-Freidrichs-Levy (CFL) limit will be used in the numerical applications (see section 4):

$$\triangle t_{CFL} = c \frac{\delta}{\bar{v}_{max}} \qquad (70)$$

where δ is the voxel size and $\bar{v}_{max}$ is the maximal GND velocity.

3.4 Discrete Fourier Transform (DFT) and differentiation rules for spatial derivatives in the Fourier space

The direct and the inverse Fourier transforms are computed here by using Fast Fourier Transform (FFT) algorithm. The representative volume element (RVE) or unit cell is assumed to be periodic with spatial periods T_1, T_2 and T_3 in the x_1, x_2 and x_3 directions, respectively, and discretized by a regular rectangular grid with $N_1 \times N_2 \times N_3$ voxels with position vector $\boldsymbol{x} = (i_1\delta_1, i_2\delta_2, i_3\delta_3)$, where $i_1 = 0 \to N_1 - 1$, $i_2 = 0 \to N_2 - 1$, $i_3 = 0 \to N_3 - 1$ and δ_1, δ_2, δ_3 are the voxel sizes in the x_1, x_2 and x_3 directions. The computational grid is constituted of a total of $N_{tot} = N_1 \times N_2 \times N_3$ voxels.

In the expression of the exponential filter presented above, the discrete representation of $\boldsymbol{\eta}_d$ is taken to be $\mathbf{m}_d/N_d$ (Gottlieb and Hesthaven, 2001). Therefore, the exponential filter for a three-dimensional computational grid is parametrized by β and p as:

$$\kappa\left(\frac{m_1}{N_1}, \frac{m_2}{N_2}, \frac{m_3}{N_3}\right) = \exp\left(-\beta\left(\left(\frac{m_1}{N_1}\right)^{2p} + \left(\frac{m_2}{N_2}\right)^{2p} + \left(\frac{m_3}{N_3}\right)^{2p}\right)\right). \qquad (71)$$

where m_j ($j = 1 \to 3$) are arranged in Fourier space as follows (Moulinec and Suquet, 1998):

$$m_j = \left(\left(-\frac{N_j}{2} + 1\right), \left(-\frac{N_j}{2} + 2\right), ..., -1, 0, 1, ..., \left(\frac{N_j}{2} - 1\right), \left(\frac{N_j}{2}\right)\right) \qquad (72)$$

28

if N_j is even, and

$$m_j = \left(\left(-\frac{N_j - 1}{2} \right), ..., -1, 0, 1, ..., \left(\frac{N_j - 1}{2} \right) \right) \tag{73}$$

if N_j is odd.

According to Moulinec and Suquet (1994, 1998), the classical approximation of the partial first derivative with respect to x_j is defined as:

$$\mathrm{i}\xi_j = \mathrm{i}\frac{2\pi}{T_j}m_j \tag{74}$$

In this paper, this approximation is not used to consider the modified Green tensor in the Lippmann-Schwinger equation or the curl operator because it was shown (Willot and Pellegrini, 2008; Berbenni et al., 2014; Lebensohn and Needleman, 2016; Djaka et al., 2017) that this approximation may lead to spurious oscillations in inhomogeneous media near material discontinuities, dislocations and when slip gradients are constrained by interfaces.

The calculation of the modified Green tensor in the Lippmann-Schwinger equation is performed using a centered finite difference scheme on a rotated grid introduced by Willot (2015). In this scheme, the first order partial derivative operator in the Fourier space is obtained as follows. First, the displacement field is expressed in the Fourier space at the four corners (in two dimensions) of a voxel in a 45° rotated basis with respect to the original Cartesian basis. The corresponding stress/strain fields are obtained in the center of the voxel in the 45° rotated basis using centered finite difference. Such stress/strain fields are expressed back in the original Cartesian basis, and then casted in the real space through the inverse DFT. The details of the method were reported in Willot (2015). Hence, the corresponding multiplier in the Fourier space between continuous and discrete Fourier transform for partial derivative of

first order can be easily deduced as follows:

$$i\xi_j^R = \frac{i}{4\delta}\tan\left(\frac{\pi m_j}{N_j}\right)\left(1 + \exp\left(i\frac{2\pi m_1}{N_1}\right)\right)\left(1 + \exp\left(i\frac{2\pi m_2}{N_2}\right)\right)\left(1 + \exp\left(i\frac{2\pi m_3}{N_3}\right)\right)$$

$$(75)$$

where m_j is defined with eqs. 72 or 73. The accuracy of such centered finite difference approximation on a rotated grid was successfully tested by Willot (2015) for inhomogeneous elastic media and by Djaka et al. (2017) for static FDM in heterogeneous media.

Following Berbenni et al. (2014), Lebensohn and Needleman (2016) and Djaka et al. (2017), the differentiation rule for the term $i\xi_k e_{jkl}(\widehat{L_{il}^p})$ in eq. 67 is based on a centered finite difference scheme (no rotated grid was needed for this term to have enough accuracy) such that the corresponding multipliers in the Fourier space between continuous and discrete Fourier transforms for partial derivative of first order reads:

$$i\xi_j^C = \frac{i}{\delta_j}\sin\left(\frac{2\pi m_j}{N_j}\right)$$

$$(76)$$

where, m_j are defined with Eqs. 72 or 73.

4 Application to the deformation of two-phase laminate microstructures: results and discussion

In the following, two different models will be investigated and discussed for periodic laminate microstructures with elastic and plastic phases (Fig. 3). A first approach, to be called here CP-EVPFFT, is based on the conventional crystal plasticity EVPFFT method where excess dislocation densities $\boldsymbol{\alpha}$ are disregarded in the above equations and follows the initial formulation developed by Lebensohn et al. (2012). A second approach, to be called here MFDM-EVPFFT, is based on the MFDM crystal plasticity model where excess dislocation (GND) densities $\boldsymbol{\alpha}$ were considered as described previously. The objective of this application is to show the numerical feasibility and stability of the FFT-based schemes presented in section 3 for a simple two-phase microstructure and the role of material parameters on the model predictions. Moreover, the role of interfacial jump condition discussed in section 2.4 will be also investigated.

4.1 Material and simulation parameters

In the following numerical simulations, a two-phase periodic laminate composite is considered to have a purely elastic phase (called *second phase*) and an elasto-viscoplastic phase (called *plastic channels*). The period of the composite in the y-direction (corresponding to $\mathbf{e}_2$) is denoted H and $H = s + 2h$ where s is the plastic channel size and $2h$ is the total size of elastic second phase along the y-direction. Elasticity is assumed to be isotropic and homogeneous with Young's modulus $E = 69 GPa$ and Poisson ratio $\nu = 0.33$ for Aluminium (Al). Therefore, the elastic shear modulus is $\mu = 25.9 GPa$. For plastic channels, the material parameters related to slip rule, GND velocity ($\dot{\gamma}^0$, m and η) and hardening model (τ_0, τ_s, θ_0 and

k_0) were consistent with pure Al. However, a specific fit to experimental data has not been carried out. The Burgers vector magnitude for Al is $b = 2.86 \times 10^{-10} m$. Since the composite effect or volume fraction effect is not investigated and only the channel size effect is studied, the volume fraction of second phase is always fixed to $f = 2h/H = 0.3125$ for all simulations. The reference material parameters used for next simulations are reported in Table 1. Among these parameters, the influence of material parameter k_0 will be investigated in the next examples. As reference parameter, k_0 is chosen following the value fitted by Acharya and Beaudoin (2000) for the case of FCC metals, i.e. $k_0 = 20$.

The unit cell is submitted to a pure shear loading with mixed strain/stress boundary conditions and applied shear strain rate $\dot{E}_{13} = \dot{E}_{31} = 0.001 s^{-1}$. The crystallographic orientation of the plastic single crystal channel is given by the three Bunge-Euler angles: $\phi_1 = 300°$, $\phi = 54.7358°$, $\phi_2 = 45°$ so that a predominant single slip mode corresponding to the slip system $(111) < 10\bar{1} >$ is activated in the channel. As a result, a Schmid factor of 0.5 is obtained for this single crystalline orientation under this specific shear loading. In this configuration, using the MFDM model, the main GND density created during this shear loading is due to screw dislocations extended along the x- direction (along $\mathbf{e}_1$) corresponding to a α_{11} dislocation density component. The MFDM theory should predict a progressive accumulation of such GND density in the course of plastic deformation, particularly important near the elastic / plastic interfaces.

Table 1

List of reference material parameters used for simulations

E (GPa)	ν	$\dot{\gamma}^0 (s^{-1})$	m	η	b (m)	τ_0 (MPa)	τ_s (MPa)	θ_0 (MPa)	k_0
69	0.33	1	0.05	0.33	2.86×10^{-10}	3	12	150	20

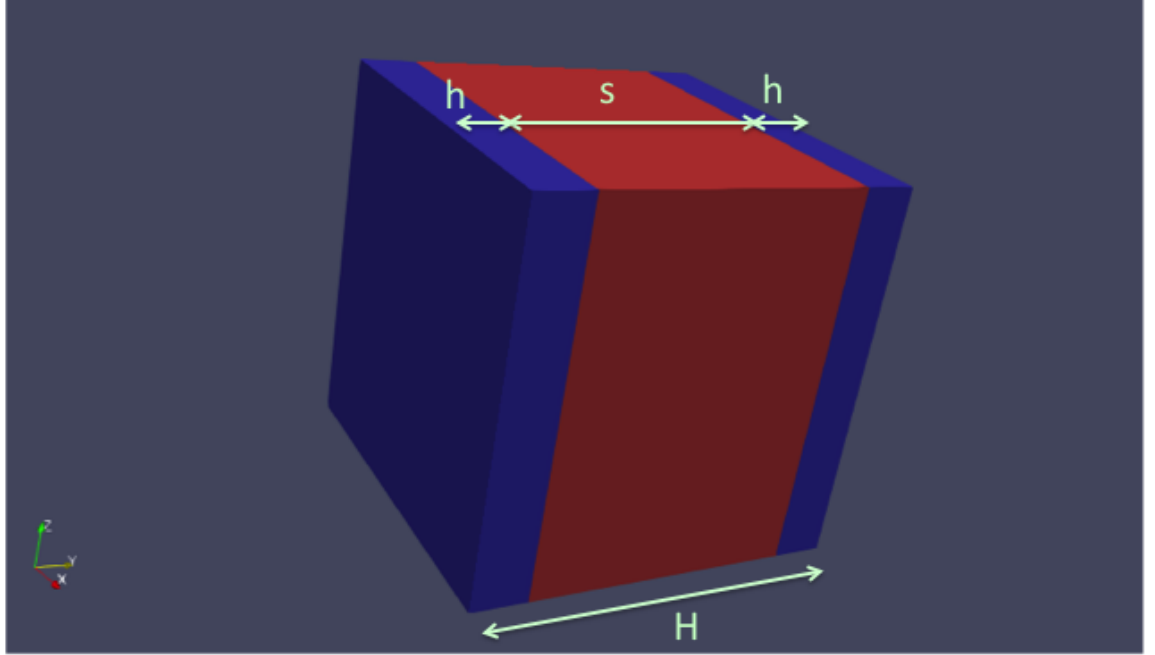The specific numerical parameters used for GND density transport equation are

Figure 3. Two-phase laminate microstructure with plastic channel (red colored) and elastic second phase (blue colored) in Cartesian coordinates.

taken from a previous study (Djaka et al., 2015) where these parameters were optimized (see Table 2).

Table 2

Numerical parameters for the spectral resolution of GND density transport equation

c	ε_M	p
0.25	0.2	1

The new numerical algorithm MFDM-EVPFFT contains some modifications with respect to the CP-EVPFFT (Lebensohn et al., 2012) that are briefly explained now. The time step is given as $\triangle t = \min\left(\triangle t_{CFL}, \triangle t_\varepsilon\right)$ where $\triangle t_{CFL}$ was defined in

eq. 70 and the time step $\triangle t_\varepsilon$ is the classic time step used in CP-EVPFFT (here for $\dot{E}_{13} = \dot{E}_{13} = 0.001s^{-1}$, $\triangle t_\varepsilon = 0.01s$). For a given time during the simulation, the explicit dislocation density transport equation is solved using eq. 69 to give the new dislocation density tensor, which is used in the GND velocity and in the strain-hardening model (eq. 30). The FFT-resolution of the Lippmann-Schwinger used a DFT-scheme coupled to a rotated centered finite difference scheme (see section 3.4). It was also seen that the new derivations reported in section 3.2 for the MFDM-EVPFFT formulation do not modify the number of Newton-Raphson iterations needed for numerical convergence of the augmented Lagrangian scheme in comparison with the CP-EVPFFT. For these simulations using isotropic homogeneous elasticity and with a quasi-linear overall hardening, these ones did not exceed four iterations to have a same accuracy as in Lebensohn et al. (2012).

4.2   Voxel refinement study

A voxel refinement study was first performed in order to adopt an optimal numerical resolution for the simulations of size effects and for the next simulation results. For the case of a unit cell with three different periods: $H = 0.0625\mu m$, $H = 0.25\mu m$ and $H = 1\mu m$, the application of the MFDM-EVPFFT formulation for the studied configuration introduced in section 4.1 leads to a clear size effect (Fig. 4) on the overall shear flow stress response of the composite $\Sigma_{13} = < \sigma_{13} >$ as a function of applied shear strain $E_{13} = < \varepsilon_{13} >$.

For this composite, it is observed that the size effect on overall flow stress is not dependent on the voxel size, i.e. the resolution of the computational grid (see Fig. 4)). According to Fig. 4, the overall response of the composite is almost not modified for each period when the cell dimension varies from $32 \times 32 \times 32$ to $128 \times 128 \times 128$ voxels, which demonstrates the rapid convergence of the stress/strain response of
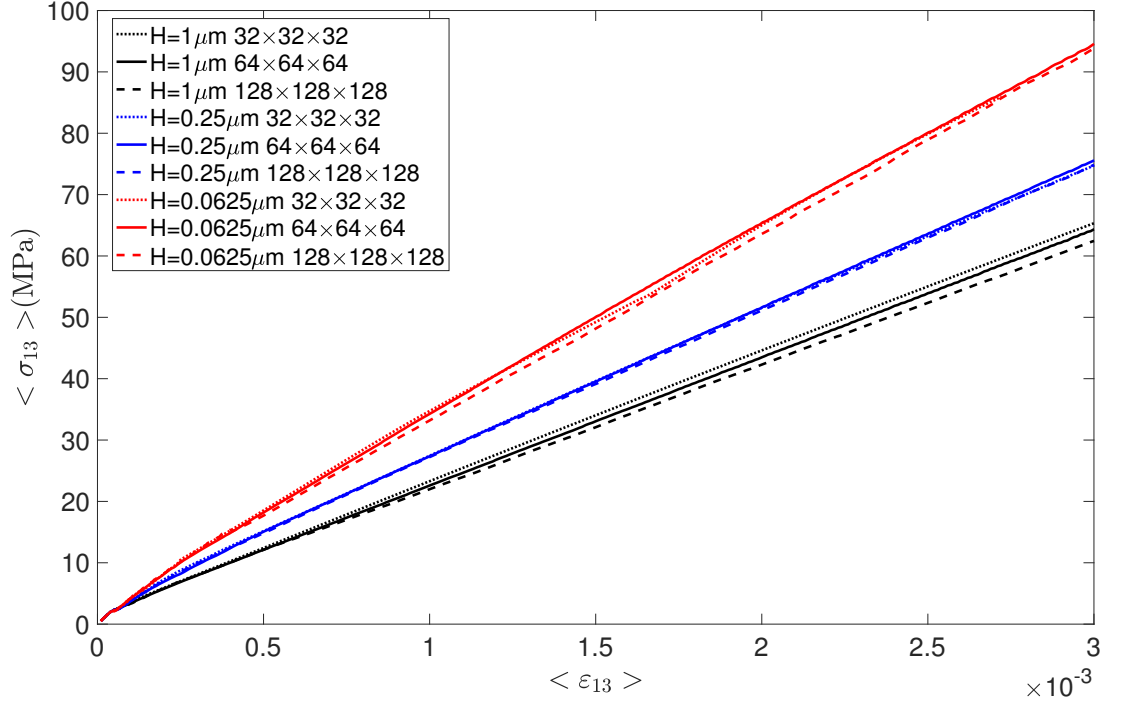
Figure 4. Overall shear stress/ shear strain responses for three different periods: $H = 0.0625\mu m$, $H = 0.25\mu m$ and $H = 1\mu m$ obtained from the MFDM-EVPFFT formulation considering three different cell dimensions: $32 \times 32 \times 32$, $64 \times 64 \times 64$ and $128 \times 128 \times 128$ voxels.

the composite. For $H = 0.25\mu m$, the local shear stress σ_{13} distributions and the internal shear stress profiles $\sigma_{13} - <\sigma_{13}>$ obtained from MFDM-EVPFFT model at 0.2% of macroscopic shear strain are reported on Fig. 5 for two different resolutions: $64 \times 64 \times 64$ and $128 \times 128 \times 128$ voxels. This example shows that similar profiles and magnitudes are obtained for the mechanical fields for both resolutions. Therefore, from the overall stress/strain responses and local stress field profiles, it is not needed to consider a voxel refinement up to a unit cell with $128 \times 128 \times 128$ voxels to predict the channel size dependent composite's mechanical response. A good compromise in terms of accuracy and CPU time for next simulations is the choice of a unit cell dimension using only $64 \times 64 \times 64$ voxels.
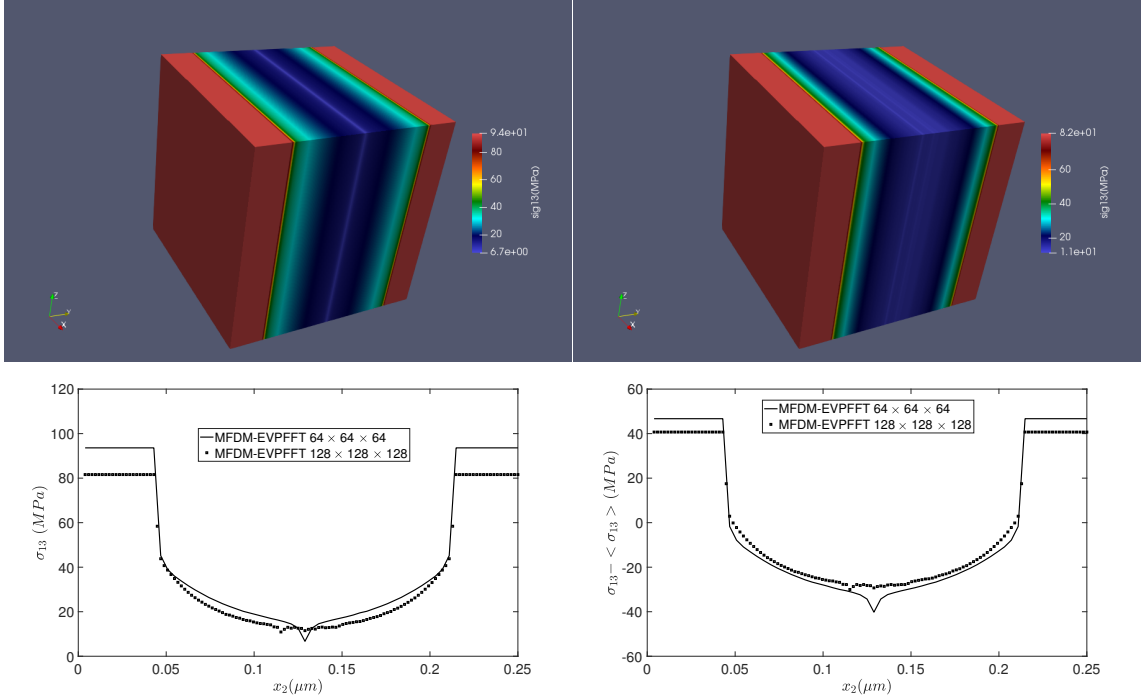
Figure 5. Distributions in local shear stress σ_{13} (in MPa) obtained from MFDM-EVPFFT at 0.2% of macroscopic shear strain for two different resolutions: $64 \times 64 \times 64$ voxels (top left) and $128 \times 128 \times 128$ voxels (top right). Shear stress σ_{13} (bottom left) and internal shear stress $\sigma_{13}- < \sigma_{13} >$ (bottom right) profiles along the $y-$direction at 0.2% of macroscopic shear strain for the two previous cell dimensions.

4.3 Channel size-dependent responses predicted by MFDM-EVPFFT formulation

Five plastic channel sizes were considered, ranging from $s = 0.043 \mu m$ to $s = 429.71 \mu m$. For all sizes, a constrained interface with jump condition was applied with the MFDM-EVPFFT formulation. In contrast with the CP-EVPFFT formulation, which is size independent considering either unconstrained or constrained interface (i.e. $[\mathbf{L^p}] \times \mathbf{n} = 0$), a channel size effect is successfully predicted with the MFDM-EVPFFT formulation. This result is consistent with Roy and Acharya (2006) and Puri et al. (2010) who provided dimensionless arguments for size scale dependence with the MFDM theory. Here, this size effect is essentially dependent on the dimensionless parameter b/s since no initial excess dislocation density tensor $\boldsymbol{\alpha}_0$

36

was prescribed as an input of these simulations. As it will be shown in the next results, the size scale dependence on the shear flow stress is due to the self-organisation of a screw double-ended GND pile up forming in the course of plastic deformation, which originates from dislocation mobility and strain-hardening in the channel constrained by elastic second phase. For the chosen default material parameters reported in Table 1, the predicted scaling law obtained with the MFDM-EVPFFT model for the overall shear flow stress at 0.2% of overall shear strain $E_{13} = <\varepsilon_{13}>$ writes as follows: $<\sigma_{13}> = <\sigma_{13}^\infty> + Ks^n$, where $n = -0.5$, $K = 6.295 MPa.\mu m^{0.5}$ and $<\sigma_{13}^\infty> \simeq 35 MPa$ is the size-independent flow stress given by the CP-EVPFFT model assuming a constrained interface. Therefore, for the studied configuration, this size dependence is closer to Hall-Petch's than Orowan's type behavior for two-phase laminate microstructures as discussed for example in Cordero et al. (2010, 2012). As reported in Fig. 4, this scaling law is not dependent on voxel size and optimized resolution with $64 \times 64 \times 64$ voxels was used. Furthermore, the predictions of the MFDM-EVPFFT model for two-phase periodic laminate structures under shear loading gives a more realistic estimate than the higher order strain gradient plasticity (SGP) model proposed by Aifantis (1987) or by Gurtin (2002). Indeed, for the latter, a constant scaling exponent $n = -2$ was reported for similar periodic microstructures in Cordero et al. (2010).
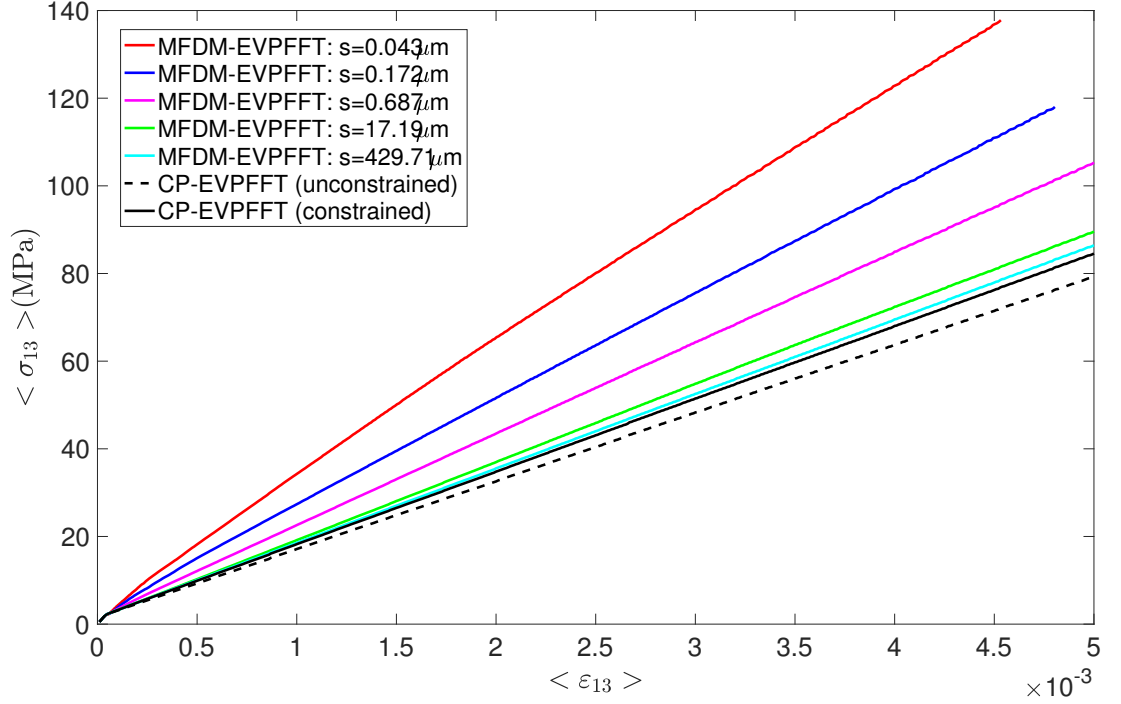
Figure 6. Channel size-dependent responses for five plastic channel sizes ranging from $s = 0.043\mu m$ to $s = 429.71\mu m$ predicted by the MFDM-EVPFFT model. Comparison with CP-EVPFFT size-independent responses assuming constrained interface (with jump condition) and unconstrained interface (without jump condition).

4.4   Responses for constrained/ unconstrained material interface

Using the same default parameters as in Table 1, the effect of a constrained/unconstrained phase boundary (using or not the jump condition developed in section 2.4 for impenetrable grain boundaries) on the overall shear stress responses is now examined for two channel sizes represented by two different periods: $H = 0.0625\mu m$ and $H = 1\mu m$ (with $64 \times 64 \times 64$ voxels). Fig. 7 reports an increase of hardening for both channel sizes due to the application of the jump condition at the phase boundaries between elastic second phase and plastic channels. However, this non local effect due to interfacial jump condition does not produce the intrinsic size effect for self-similar microstructures as reported in section 4.3. Thus, most of the size effects come from
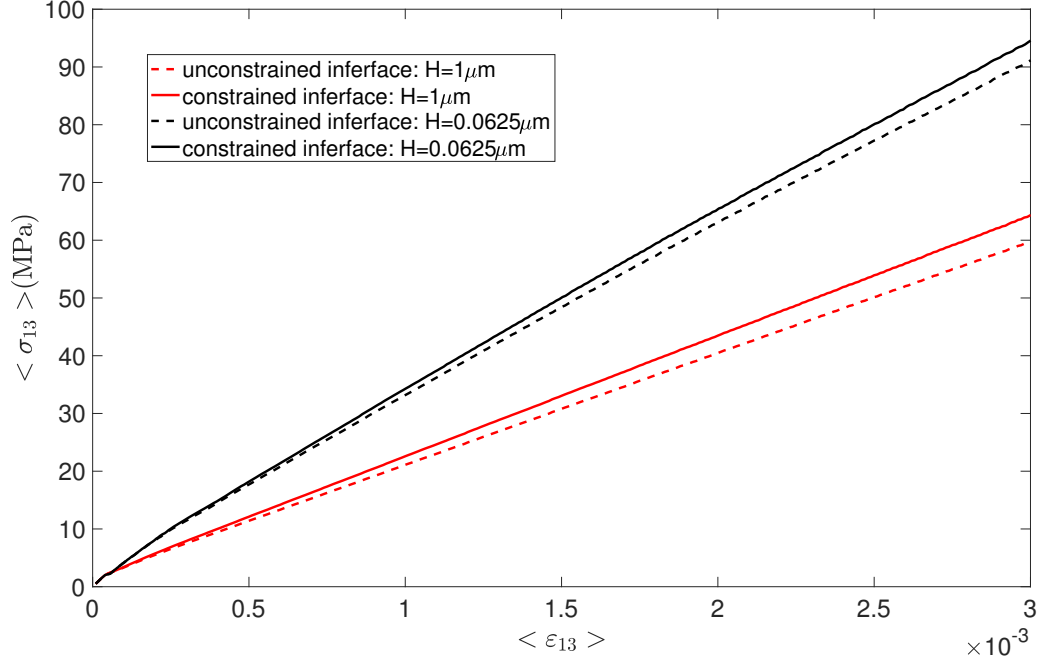
Figure 7. Effect of interfacial jump condition on the overall shear stress responses of the two-phase composite obtained from MFDM-EVPFFT for $H = 1\mu m$ and $H = 0.0625\mu m$.

the extended GND pile-ups and the resulting increase in strain hardening. In our simulations, phase boundaries are not considered as dislocation sources as done by Puri et al. (2010). This hardening effect on shear stress responses effect was already reported using FE simulations in Richeton et al. (2011) (see their figure 8 for example). In addition, the hardening effect described in Fig. 7 is less pronounced than the one observed by Puri et al. (2010) for bicrystals, where in their case two plastic crystals were considered and some comparisons were made between two extreme cases: penetrable grain boundary with slip transmission from one crystal to another and impenetrable grain boundary (slip blocked in one crystal at the grain boundary).

4.5 Plastic distortion, internal shear stress and GND density profiles in the plastic channel

In order to explain the clearly observed differences between the size-insensitive classic CP-EVPFFT model and the present MFDM-EVPFFT formulation, let us consider the spatial variation along the y-direction (see Fig. 5) of the plastic distortion U_{13}^p, the shear stress σ_{13}, the internal shear stress defined as $\sigma_{13} - <\sigma_{13}>$ and the screw GND density component α_{11} normalized by the Burgers vector magnitude b. The numerical results are reported on Figs. 8, 9 and 10 respectively considering $H = 0.25\mu m$ and an overall shear strain $E_{13} = <\varepsilon_{13}> = 0.2\%$. According to the MFDM-EVPFFT formulation, the plastic distortion (or slip) profile (see Fig. 8) exhibits a spatial gradient in the y-direction of the channel in contrast with the CP-EVPFFT model, which classically gives a uniform slip in the channel. Intra-granular slip gradients were also recently reported by Lebensohn and Needleman (2016)using a higher order non-local formulation in the EVPFFT formulation, introducing a backstress involving a length scale based on the SGP model of Gurtin (2002). For the MFDM-EVPFFT formulation, slip is maximal in the middle of the channel and gradually decreases to zero at the interfaces and in the elastic second phase (no plastic distortion). The consequences of this plastic distortion gradient is directly visible on the shear stress and and internal shear stress profiles, which also both exhibit a spatial gradient starting from the middle of the channel, see Fig. 9 and Fig. 10 respectively. The small observed cusps observed at the middle of the channel is explained by the choice of the used numerical resolution ($64 \times 64 \times 64$ voxels, see Fig. 5). However, these ones have no consequence on the composite's mechanical response as seen in Fig. 4. From the examination of the major GND density component α_{11} as a function of x_2 (Fig. 11), the GND density is important in the neighborhood of phase boundaries forming a continuous screw double-ended GND pile up. In the

center of the channel, it totally cancels due to the annihilation of two GND densities with opposite signs. In comparison, the classic CP-EVPFFT describes a dipole of screw GNDs only located at the phase boundaries. This corresponds to Frank-Bilby interfacial dislocations, which are unrealistic for this plastically deformed two-phase laminate.
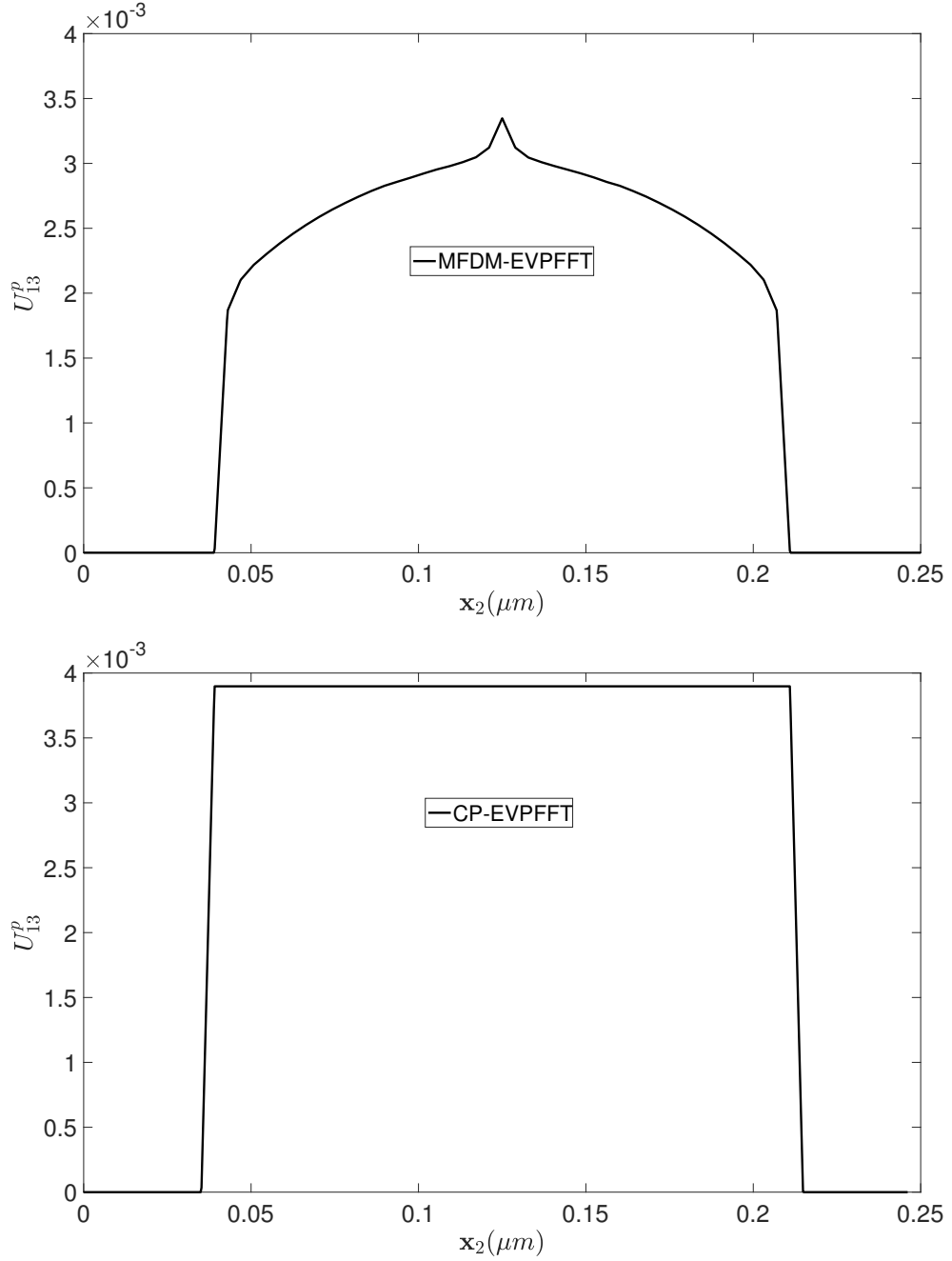
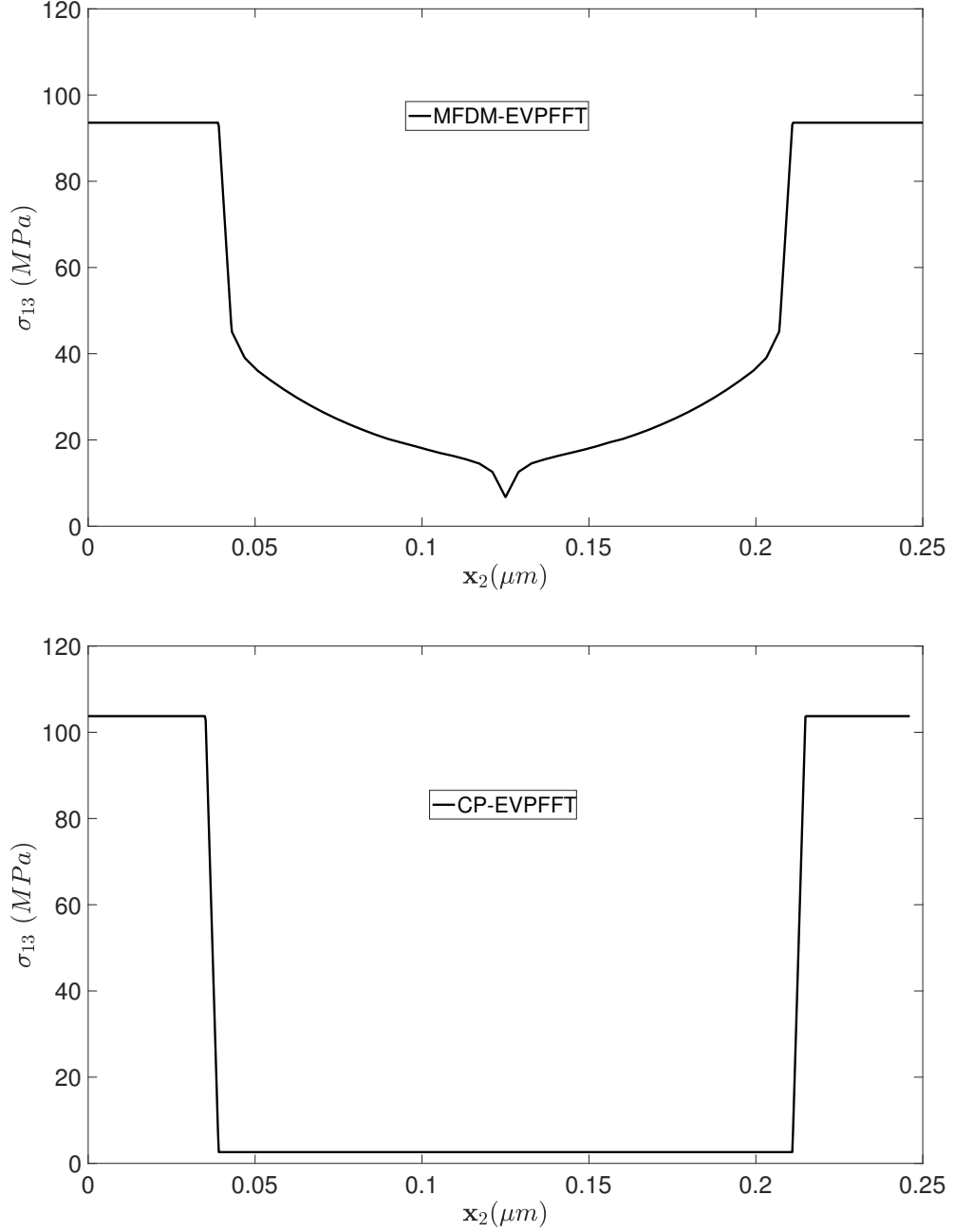Figure 8. Plastic distortion profiles U_{13}^p as a function $x_2 = y$ (i.e. along the normal to the phase boundaries) predicted by MFDM-EVPFFT (top) vs. CP-EVPFFT (bottom) formulations, for an overall shear strain $E_{13} =< \varepsilon_{13} >= 0.2\%$.

Fig. 12 reports for different steps in the simulation, namely $E_{13} = 0.1\%$, $E_{13} = 0.2\%$, $E_{13} = 0.3\%$ and $E_{13} = 0.45\%$, the time evolution of the non zero GND density components along the normal direction to the phase boundary. It can be seen as

Figure 9. Shear stress profiles σ_{13} as a function $x_2 = y$ (i.e. along the normal to the phase boundaries) predicted by MFDM-EVPFFT (top) vs. CP-EVPFFT (bottom) formulations, for an overall shear strain $E_{13} = <\varepsilon_{13}> = 0.2\%$.

expected, that the jump condition imposes a constraint on the following GND density components: $\alpha_{23} = \alpha_{21} = 0$ but not on α_{11}, α_{33}, α_{13} and α_{31} (see eq. 42). At all strains, it is clear that the major GND density component is α_{11} (screw dislocations)
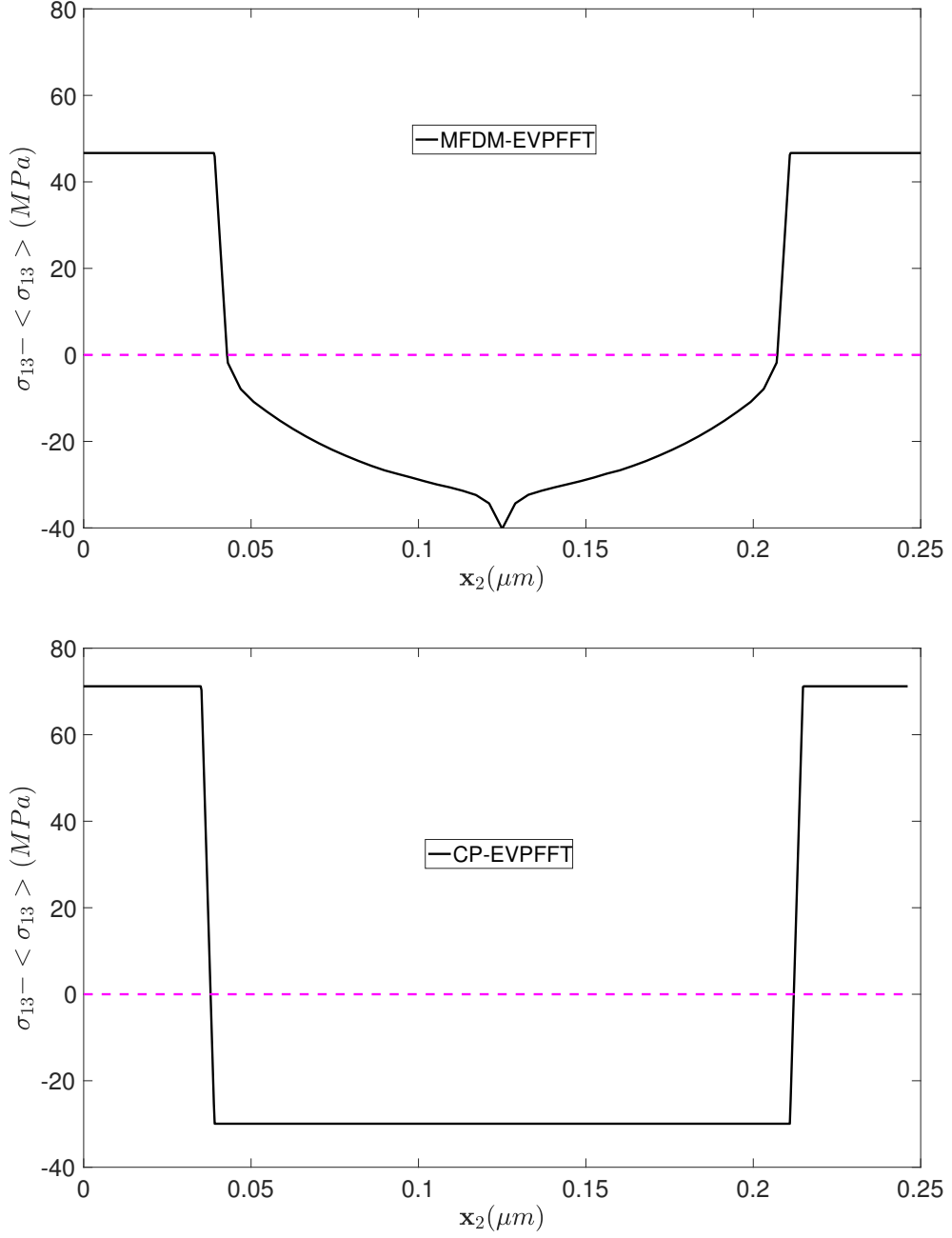
Figure 10. Internal shear stress profiles $\sigma_{13}- < \sigma_{13} >$ as a function $x_2 = y$ (i.e. along the normal to the phase boundaries) predicted by MFDM-EVPFFT (top) vs. CP-EVPFFT (bottom) formulations, for an overall shear strain $E_{13} =< \varepsilon_{13} >= 0.2\%$.

which is due to the applied shear loading (anti-plane shear with respect to the interface). It can be seen from the numerical values reported on Fig. 12 that the values of α_{11}/b are at least 1000 times larger than the other components close to the
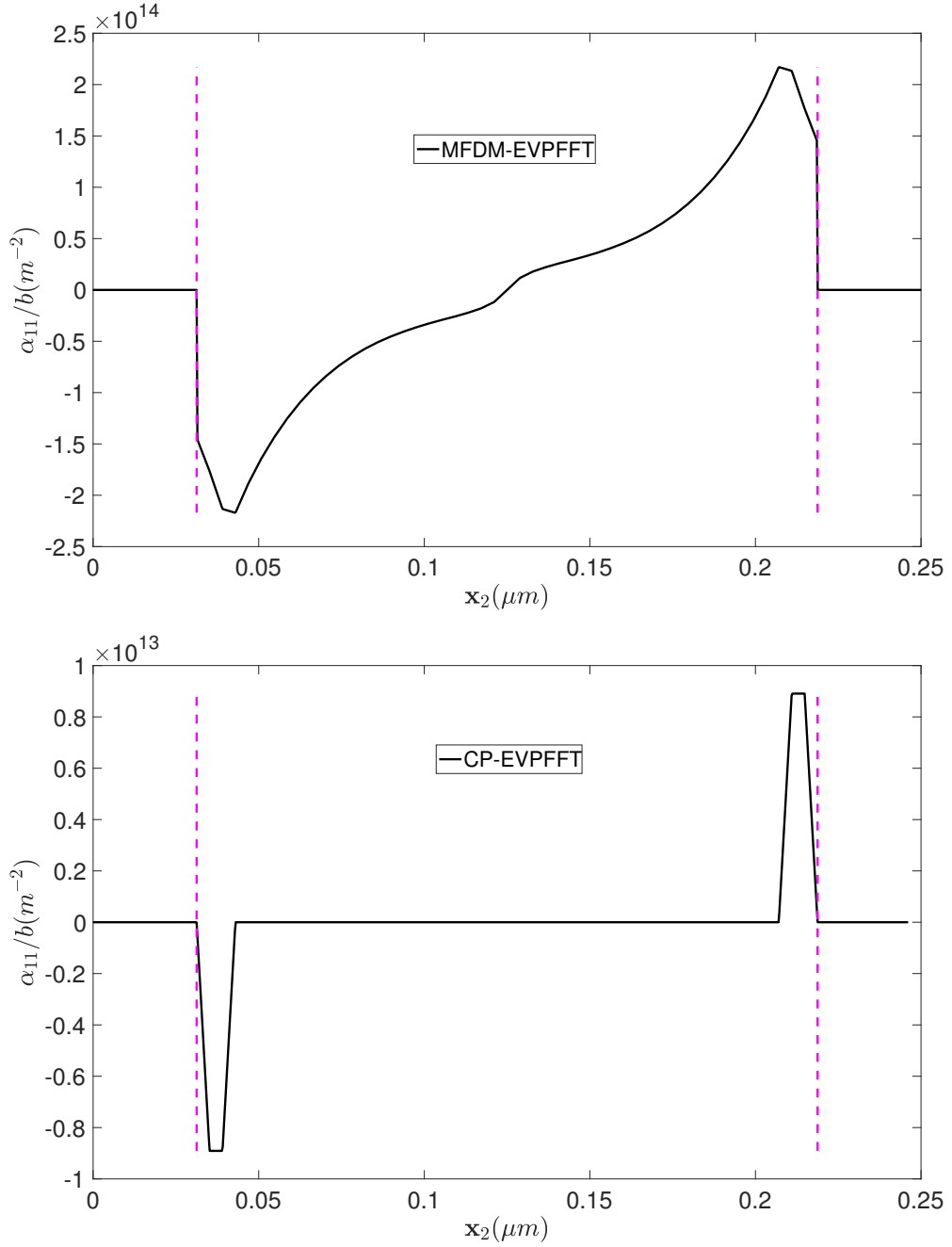
Figure 11. Profile of GND density component α_{11} normalized by b as a function $x_2 = y$ (i.e. along the normal to the phase boundaries) predicted by MFDM-EVPFFT (top) vs. CP-EVPFFT (bottom) formulations, for an overall shear strain $E_{13} = <\varepsilon_{13}> = 0.2\%$.

phase boundaries. However, the spatial variation of GND density fields as obtained here from the spectral resolution of the dislocation density transport equation (see section 3.3) in a reduced version of the MFDM theory (Roy et al., 2007) is seen to
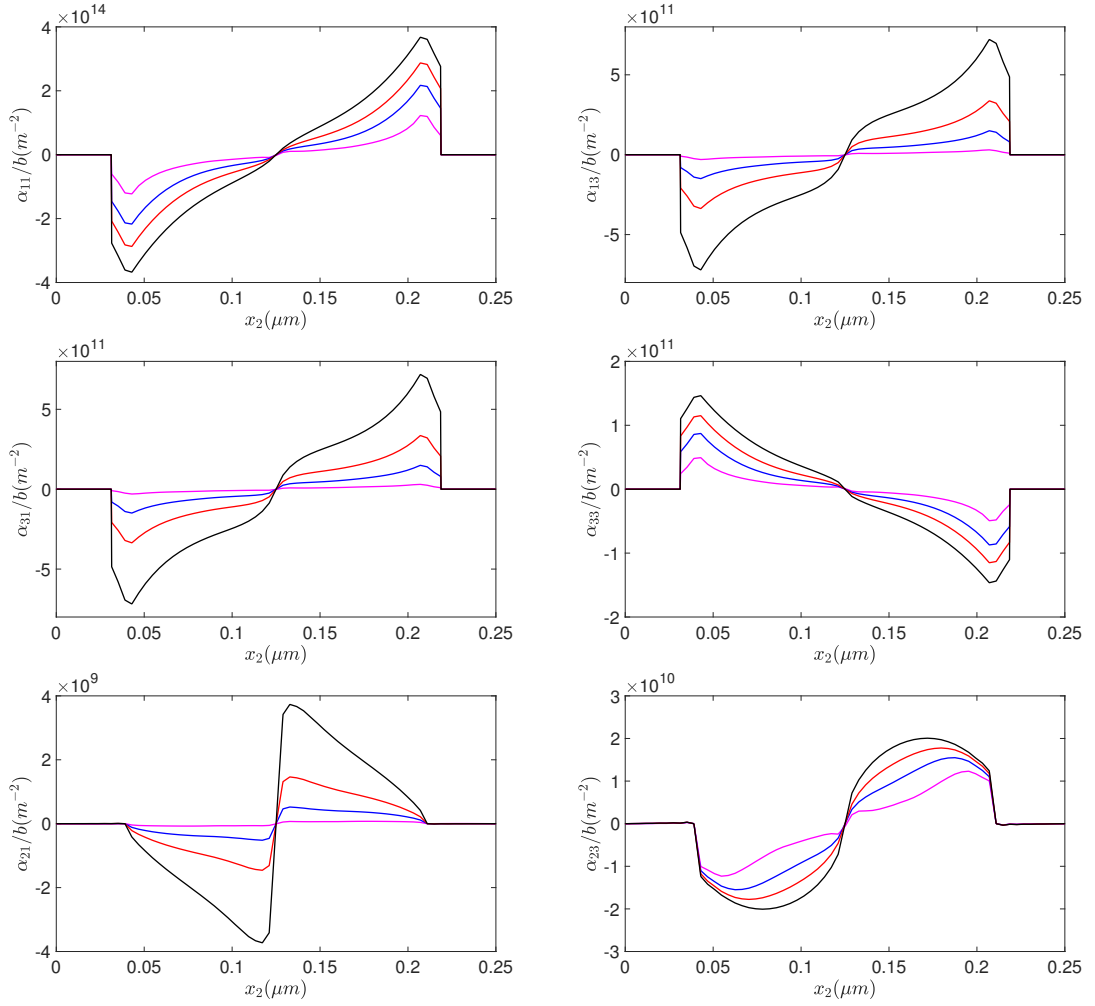
Figure 12. Time evolution of the different non zero GND densities normalized by b as a function of applied shear strain: $E_{13} = 0.1\%$ (magenta), $E_{13} = 0.2\%$ (blue), $E_{13} = 0.3\%$ (red) and $E_{13} = 0.45\%$ (black).

be smoother near interface that the fields obtained from $\boldsymbol{\alpha} = -\mathbf{curl}\ \mathbf{U}^p$ after the numerical implementation of the integration of eq. 10. A numerical improvement in this direction can be envisaged implementing the full equations of the MFDM theory as reported in Acharya and Roy (2006) (see their eqs. 23) in the present MFDM-EVPFFT formulation.

46

4.6 Parameter study of the influence of k_0 on the mechanical response of the composite

Lastly, let us consider the influence of material parameter k_0 on the mechanical responses of the two-phase composite. This physical parameter is important since it defines the mean free path of GND (see section 2.2, eq. 31). The effect of k_0 on the overall shear stress responses is reported on Fig. 13 considering three different values: $k_0 = 10$, $k_0 = 20$, $k_0 = 40$. It is shown that an increase of k_0 leads to an increase of the flow stress for a same shear strain. For these three different values of k_0, a scaling law with $n \simeq -0.5$ is observed. Considering now the particular case of $H = 0.25 \mu m$, i.e. $s = 0.172 \mu m$, comparisons of the different mechanical fields for these three different values of k_0 are given in Fig. 14. It is seen that plastic distortion gradient and internal stress gradient are slightly stronger for larger values of k_0. When k_0 is decreased from $k_0 = 40$ to $k_0 = 10$, the cusps observed at the centre of the channel become less visible. This local hardening effect observed in Fig. 13 due to an increase of k_0 is enhanced by a decrease of the mean free path of GND. In the regions where the GND density is higher (i.e. in the neighborhood of phase boundaries), local hardening becomes stronger because the mean free path of GND scales with the inverse of $|\boldsymbol{\alpha} \cdot \mathbf{n}^s|$ (see eq. 31).
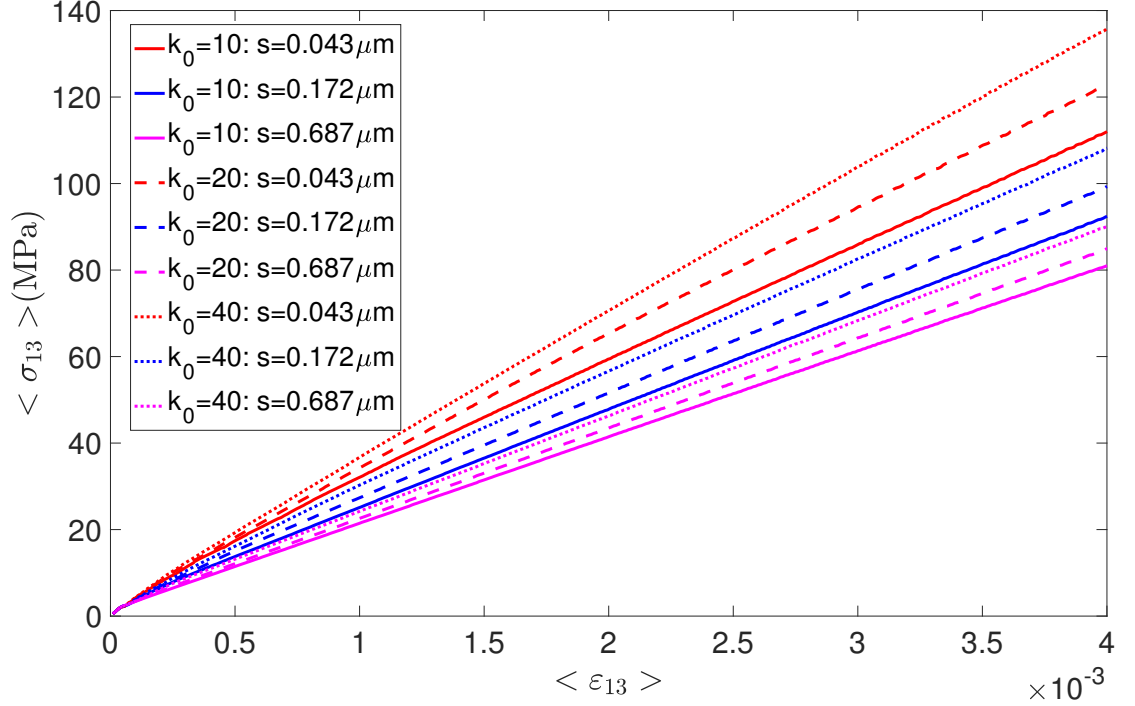
Figure 13. Channel size-dependent responses for three plastic channel sizes from $s = 0.043\mu m$ (red) to $s = 0.687\mu m$ (magenta) predicted by the MFDM-EVPFFT model for three different values of material parameter k_0 involved in the mean free path of GND: $k_0 = 10$ (solid lines), $k_0 = 20$ (dotted lines), $k_0 = 40$ (dashed lines).

5 Summary and outlook

A new spectral formulation called MFDM-EVPFFT was developed to extend the EVPFFT formulation (Lebensohn et al., 2012) to a reduced version of Mesoscale Field Dislocation Mechanics that includes GND and SSD effects (Acharya and Roy, 2006). As in the case of the finite element implementation of the MFDM theory, the present FFT-based approach is able to successfully describe realistic channel size effects for the mechanical response of two-phase laminate microstructures with elastic second phase and plastic channels. The MFDM-EVPFFT is based on five new features as compared to the CP-EVPFFT formulation:

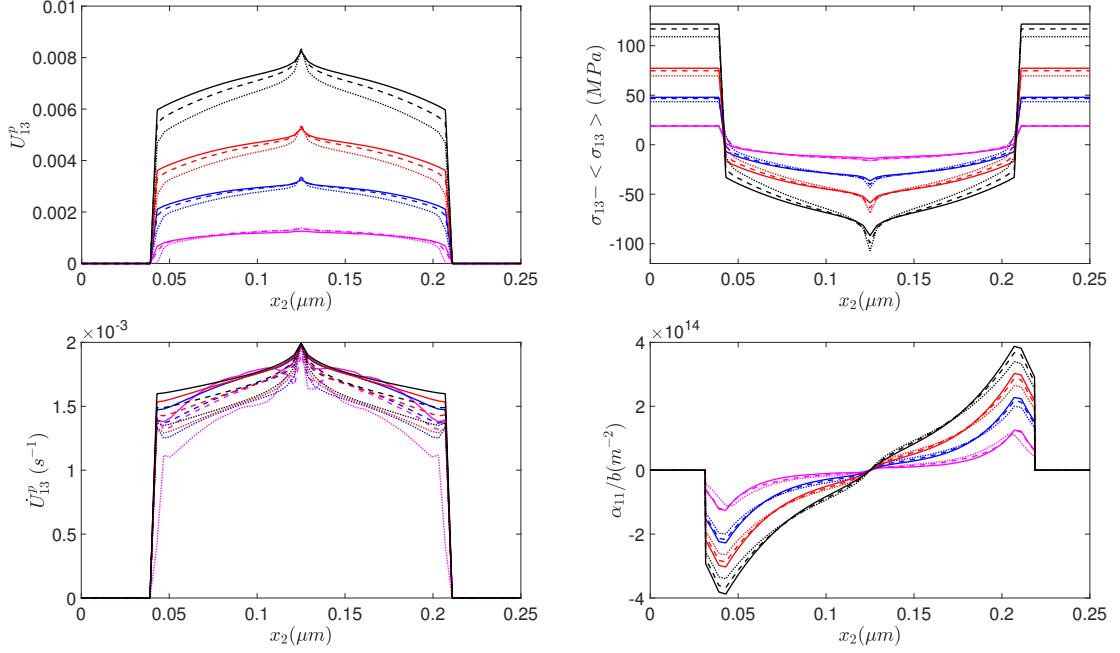- a new expression of the Jacobian for the augmented Lagrangian scheme consider-

Figure 14. Effect of k_0 on different mechanical fields for $k_0 = 10$ (solid lines), $k_0 = 20$ (dotted lines), $k_0 = 40$ (dashed lines): U_{13}^p (top left), $\sigma_{13} - <\sigma_{13}>$ (top right), $\dot{U}_{13}^p$ (bottom left), α_{11}/b (bottom right) at different shear strains: $E_{13} = 0.1\%$ (magenta), $E_{13} = 0.2\%$ (blue), $E_{13} = 0.3\%$ (red) and $E_{13} = 0.45\%$ (black).

ing plastic strain rate due to GNDs in addition to the one due to SSDs;

- a numerical spectral resolution of the dislocation density transport equation coupled to stress equilibrium;

- a hardening rule accounting for GND densities with effects on SSD and GND mobilities;

- a jump condition on plastic distortion rate describing the conservation of Burgers vector content at material discontinuities between plastic channels and elastic second phase;

- a spectral discrete method based on finite difference schemes to treat both lattice incompatibility and integral Lippmann-Schwinger equations.

In this non local formulation, this size scale dependence is closely related to the generation of continuous dislocation pile-ups from the centre of channels to phase

boundaries, which are not captured by a classic CP-EVPFFT describing only interfacial GND constrained at phase boundaries. The present MFDM-EVPFFT model is different from the higher order Strain Gradient Plasticity (SGP)-EVPFFT (Lebensohn and Needleman, 2016), which is formulated in terms of dissipative and energetic hardening included in the constitutive equations. However, both approaches revealed slip gradients and size effects that can be calibrated using the material parameters of the constitutive models. For the MFDM-EVPFFT model, it is shown that both GND densities and slip constraint at phase boundaries influence the overall and local hardening behaviors as well as the calibration of the mean free path of GND through a material parameter that can be fitted with experiments.

Many other applications can now be pursued, after this first implementation of the MFDM-EVPFFT formulation. Here, a reduced version of the MFDM theory was used, which can be improved by a future implementation of the full equations of the MFDM theory (Acharya and Roy, 2006) in the MFDM-EVPFFT formulation. Furthermore, a study of the Bauschinger effect can be performed considering reversible and cyclic plasticity to quantify the effects GND polarity and mobility on kinematic hardening. Also, the present MFDM-EVPFFT model can be applied to polycrystals with different grain sizes under different slip assumptions at grain boundaries (forthcoming paper is in preparation). Finally, since robust FFT-based solvers for crystal elasto-viscoplasticity at finite strains are now available (Eisenlohr et al., 2013; Shanthraj et al., 2015), the MFDM-EVPFFT can also be extended to a large deformation framework using the finite deformation FDM equations (Acharya, 2004).

Acknowledgements

References

Acharya, A., 2001. A model of crystal plasticity based on the theory of continuously distributed dislocations. Journal of the Mechanics and Physics of Solids 49, 761 – 784.

Acharya, A., 2003. Driving forces and boundary conditions in continuum dislocation mechanics. Proceedings of the Royal Society London A 459, 1343–1363.

Acharya, A., 2004. Constitutive analysis of finite deformation field dislocation mechanics. Journal of the Mechanics and Physics of Solids 52, 301 – 316.

Acharya, A., 2007. Jump condition for gnd evolution as a constraint on slip transmission at grain boundaries. Philosophical Magazine 87, 1349–1359.

Acharya, A., 2011. Microcanonical entropy and mesoscale dislocation mechanics and plasticity. Journal of Elasticity 104, 23–44.

Acharya, A., Bassani, J. L., 2000. Lattice incompatibility and a gradient theory of crystal plasticity. Journal of the Mechanics and Physics of Solids 48(8), 1565–1595.

Acharya, A., Beaudoin, A. J., 2000. Grain size effect in viscoplastic polycristals at moderate strains. Journal of the Mechanics and Physics of Solids 48, 2213 – 2230.

Acharya, A., Roy, A., 2006. Size effects and idealized dislocation microstructure at small scales : Predictions of a Phenomenological model of Mesoscopic Field Dislocation Mechanics : Part I. J. Mech. Phys. Solids 54, 1687–1710.

Acharya, A., Roy, A., Sawant, A., 2006. Continuum theory and methods for coarse-

grained plasticity. Scripta Mater. 54, 705–710.

Aifantis, E. C., 1984. On the microstructural origin of certain inelastic models. Trans. ASME J. Eng. Mater. Technol. 106, 326–330.

Aifantis, E. C., 1987. The physics of plastic deformation. International Journal of Plasticity 3, 211–247.

Aifantis, K. E., Willis, J. R., 2005. The role of interfaces in enhancing the yield strength of composites and polycrystals. Journal of the Mechanics and Physics of Solids 54, 5077–5085.

Anglin, B. S., Lebensohn, R. A., Rollett, A. D., 2014. Validation of a numerical method based on fast Fourier transforms for heterogeneous thermoelastic materials by comparison with analytical solutions. Computational Materials Science 87, 209–217.

Arsenlis, A., Parks, D. M., 1999. Crystallographic aspects of geometrically necessary and statistically stored dislocation density. Acta Mater. 47, 1597–1611.

Arsenlis, A., Parks, D. M., 2002. Modeling the evolution of crystallographic dislocation density in crystal plasticity. Journal of the Mechanics and Physics of Solids 50, 1979–2009.

Ashby, M. F., 1970. Deformation of plastically non-homogeneous materials. Philosophical Magazine 21, 399–424.

Barbe, F., Decker, L., Jeulin, D., Cailletaud, G., 2001. Intergranular and intragranular behavior of polycrystalline aggregates. Part 1: F.E. model. International Journal of Plasticity 17, 513–536.

Bassani, J. L., 2001. Incompatibility and a simple gradient theory of plasticity. Journal of the Mechanics and Physics of Solids 49, 1983–1996.

Bassani, J. L., Needleman, A., VanderGiessen, E., 2001. Plastic flow in a composite: a comparison of nonlocal continuum and discrete dislocation predictions. International Journal of Solids and Structures 38, 833–853.

Berbenni, S., Taupin, V., 2018. Fast Fourier Transform-based micromechanics of interfacial line defects in crystalline materials. Journal of Micromechanics and Molecular Physics 1840007, doi:10.1142/S2424913018400076.

Berbenni, S., Taupin, V., Djaka, K. S., Fressengeas, C., 2014. A numerical spectral approach for solving elasto-static field dislocation and g-disclination mechanics. International Journal of Solids and Structures 51, 4157–4175.

Berbenni, S., Taupin, V., Fressengeas, C., Capolungo, L., 2016. A fast Fourier transform-based approach for generalized disclination mechanics within a couple stress theory. Generalized Continua as Models for Classical and Advanced Materials, Advanced Structured Materials, H. Altenbach and S. Forest (eds.), Springer International Publishing Switzerland, 47–75.

Bertin, N., Capolungo, L., 2018. A FFT-based formulation for discrete dislocation dynamics in heterogeneous media. Journal of Computational Physics 355, 366–384.

Bertin, N., Upadhyay, M. V., Pradalier, C., Capolungo, L., 2015. A FFT-based formulation for efficient mechanical fields computation in isotropic and anisotropic periodic discrete dislocation dynamics. Modelling and Simulation in Materials Science and Engineering 23, 065009.

Bittencourt, E., Needleman, A., Gurtin, M. E., VanderGiessen, E., 2003. A comparison of non local continuum and discrete dislocation plasticity predictions. Journal of the Mechanics and Physics of Solids 51, 281–310.

Brenner, R., Beaudoin, A. J., Suquet, P., Acharya, A., 2014. Numerical implementation of static Field Dislocation Mechanics theory for periodic media. Philosophical Magazine, 1–24.

Brenner, R., Lebensohn, R. A., Castelnau, O., 2009. Elastic anisotropy and yield surface estimates of polycrystals. International Journal of Solids and Structures 46, 3018–3026.

Brisard, S., Dormieux, L., 2010. Fft-based methods for the mechanics of composites: A general variational framework. Comp. Mater. Sci. 49, 663–671.

Brisard, S., Dormieux, L., 2012. Combining galerkin approximation techniques with the principle of Hashin and Shtrikman to derive a new FFT-based numerical method for the homogenization of composites. Comput. Methods Appl. Mech. Engrg 217-220, 197–212.

Cailletaud, G., Forest, S., Jeulin, D., Feyel, F., Galliet, I., Mounoury, V., Quilici, S., 2003. Some elements of microstructural mechanics. Computational Materials Science 27, 351–374.

Chang, H.-J., Gaubert, A., Fivel, M., Berbenni, S., Bouaziz, O., Forest, S., 2015. Analysis of particle induced dislocation structures using three-dimensional dislocation dynamics and strain gradient plasticity. Computational Materials Science 52, 33–39.

Cordero, N. M., Forest, S., Busso, E. P., Berbenni, S., Cherkaoui, M., 2012. Grain size effects on plastic strain and dislocation density tensor fields in metal polycrystals. Computational Materials Science 52, 7–13.

Cordero, N. M., Gaubert, A., Forest, S., Busso, E. P., Galerneau, F., Kruch, S., 2010. Size effects in generalised continuum crystal plasticity for two-phase laminates. Journal of the Mechanics and Physics of Solids 58, 1963–1994.

Danas, K., Deshpande, V. S., Fleck, N. A., 2010. Compliant interfaces: a mechanism for relaxation of dislocation pile-ups in a sheared single crystal. International Journal of Plasticity 26, 1792–1805.

Delaire, F., Raphanel, J. L., Rey, C., 2000. Plastic heterogeneities of a copper multicrystal deformed in uniaxial tension: experimental study and finite element simulations. Acta Materialia 48, 1075–1087.

Djaka, K. S., Taupin, V., Berbenni, S., Fressengeas, C., 2015. A numerical spectral approach to solve the dislocation density transport equation. Modelling and

Simulation in Materials Science and Engineering 23, 065008(27pp).

Djaka, K. S., Villani, A., Taupin, V., Capolungo, L., Berbenni, S., 2017. Field dislocation mechanics for heterogeneous elastic materials: A numerical spectral approach. Computer Methods in Applied Mechanics and Engineering 315, 921–942.

Donegan, S. P., Rollett, A. D., 2015. Simulation of residual stress and elastic energy density in thermal barrier coatings using fast Fourier transforms. Acta Materialia 96, 212–228.

Dreyer, W., Müller, W. H., Olschewski, J., 1999. An approximate analytical 2D-solution for the stresses and strains in eigenstrained cubic materials. Acta Mech. 136 (3-4), 171–192.

Eisenberg, M., 1970. On the relation between continuum plasticity and dislocation theories. International Journal of Engineering Science 8, 261–271.

Eisenlohr, P., Diehl, M., Lebensohn, R. A., Roters, F., 2013. A spectral method solution to crystal elasto-viscoplasticity at finite strains. Int. J. Plast. 46, 37–53.

Eloh, K. S., Jacques, A., Berbenni, S., 2018. Development of a new consistent discrete Green operator for FFT-based methods to solve heterogeneous problems with eigenstrains. International Journal of Plasticity In Press, doi:10.1016/j.ijplas.2018.10.011.

Evers, L. P., Brekelmans, W. A. M., Geers, M. G. D., 2004. Non-local crystal plasticity model with intrinsic SSD and GND effects. Journal of the Mechanics and Physics of Solids 52, 2379–2401.

Evers, L. P., Parks, D. M., Brekelmans, W. A. M., Geers, M. G. D., 2002. Crystal plasticity model with enhanced hardening by geometrically necessary dislocation accumulation. Journal of the Mechanics and Physics of Solids 50, 2403–2424.

Eyre, D. J., Milton, G. W., 1999. A fast numerical scheme for computing the response of composite using grid refinement. European Physical Journal - Applied Physics 6, 41–47.

Fleck, N. A., Hutchinson, J. W., 1993. A phenomenological theory of strain gradient plasticity. J. Mech. Phys. Solids 41, 1825–1857.

Fleck, N. A., Hutchinson, J. W., 1997. Strain gradient plasticity. Advances in Applied Mechanics 33, 295–361.

Fleck, N. A., Hutchinson, J. W., 2001. Reformulation of strain gradient plasticity. Journal of the Mechanics and Physics of Solids 48, 2245–2271.

Fleck, N. A., Hutchinson, J. W., Willis, J. R., 2015. Guidelines for constructing strain gradient plasticity theories. Trans. ASME Journal of Applied Mechanics 82, 071002–10pages.

Fleck, N. A., Willis, J. R., 2009. A mathematical basis for strain-gradient plasticity theory- Part I: scalar plastic multiplier. Journal of the Mechanics and Physics of Solids 57, 161–177.

Fox, N., 1966. A continuum theory of dislocations for single crystals. J. Inst. Math. Appl. 2, 285–298.

Gao, H., Huang, Y., Nix, W. D., Hutchinson, J. W., 1999. Mechanism-based strain gradient plasticity-i. theory. Journal of the Mechanics and Physics of Solids 47, 1239–1263.

Gottlieb, D., Hesthaven, J. S., 2001. Spectral methods for hyperbolic problems. Journal of Computational and Applied Mathematics 128, 83–131.

Graham, J. T., Rollett, A. D., LeSar, R., 2016. Fast fourier transform discrete dislocation dynamics. Modell. Simul. Mater. Sci. Eng. 8, 085005.

Grennerat, F., Montagnat, M., Castelnau, O., Vacher, P., Moulinec, H., Suquet, P., Duval, P., 2012. Experimental characterization of the intragranular strain field in columnar ice during transient creep. Acta Mater. 60, 3655–3666.

Gudmundson, P., 2004. A unified treatment of strain gradient plasticity. Journal of the Mechanics and Physics of Solids 52, 1379–1406.

Gupta, S., Beaudoin, A. J., Chevy, J., 2017. Strain rate jump induced negative

strain rate sensitivity (nsrs) in aluminium alloy 2024: Experiments and constitutive modeling. Materials Science Engineering A 683, 143–152.

Gurtin, M., 2000. On the plasticity of single crystals: free energy, microforces, plastic-strain gradients. Journal of the Mechanics and Physics of Solids 48, 989–1036.

Gurtin, M., 2002. A gradient theory of single-crystal viscoplasticity that accounts for geometrically necessary dislocations. Journal of the Mechanics and Physics of Solids 50, 5–32.

Gurtin, M., 2004. A gradient theory of small-deformation isotropic plasticity that accounts for the Burgers vector and for dissipation due to plastic spin. Journal of the Mechanics and Physics of Solids 52, 2545–2568.

Gurtin, M. E., Anand, L., 2005. A theory of strain-gradient plasticity for isotropic, plastically irrotational materials, Part I: Small deformations. Journal of the Mechanics and Physics of Solids 53, 2545–2568.

Gurtin, M. E., Anand, L., 2009. Thermodynamics applied to gradient theories involving accumulated plastic strain: The theories of Aifantis and Fleck and Hutchinson and their generalization. Journal of the Mechanics and Physics of Solids 57, 405–421.

Gurtin, M. E., Anand, L., Lele, S. P., 2007. Gradient single-crystal plasticity with free energy dependent on dislocation densities. Journal of the Mechanics and Physics of Solids 55, 1853–1878.

Gurtin, M. E., Needleman, A., 2005. Boundary conditions in small-deformation, single crystal plasticity that account for the Burgers vector. Journal of the Mechanics and Physics of Solids 53, 1–31.

Han, C. S., Gao, H., Huang, Y., Nix, W. D., 2005. Mechanism-based strain gradient crystal plasticity-i. theory. Journal of the Mechanics and Physics of Solids 53, 1188–1203.

Han, H. T., Jaunzemis, W., 1973. A dislocation theory of plasticity. International

Journal of Engineering Science 11, 1065–1078.

Kabel, M., Böhlke, T., Schneider, M., 2014. Efficient fixed point and Newton-Krylov solvers for FFT-based homogenization of elasticity at large deformations. Comp. Mech. 54 (6), 1497–1514.

Kabel, M., Fliegener, S., Schneider, M., 2016. Mixed boundary conditions for FFT-based homogenization at finite strains. Comp. Mech. 57 (2), 193–210.

Kocks, U. F., 1976. Laws for work-hardening and low-temperature creep. ASME Journal of Engineering Materials and Technology 98, 76–85.

Kosevich, A. M., 1979. Crystal dislocations and the theory of elasticity. In: Dislocations in Solids (vol. 1). Nabarrro, F.R.N. (ed.), North-Holland Publishing Company, Amsterdam, pp. 33–141.

Kröner, E., 1958. Kontinuumstheorie der Versetzungen und Eigenspannungen. Collatz L and Loesch F (eds.). Ergebnisse der Angewewandte Mathematik 5, Springer Verlag, Berlin.

Kröner, E., 1981. Continuum theory of defects. In: Physics of defects. R. Balian et al. (Eds.), Les Houches, Session 35, North Holland, New York, pp. 215–315.

Lebensohn, R., 2001. N-site modeling of a 3D viscoplatic polycrystal using Fast Fourier Transform. Acta Materialia 49, 2723–2737.

Lebensohn, R., Brenner, R., Castelnau, O., Rollett, A., 2008. Orientation image-based micromechanical modelling of subgrain texture evolution in polycrystalline copper. Acta Mater. 56, 3914–3926.

Lebensohn, R., Escobedo, J., Cerreta, E., Dennis-Koller, D., Bronkhorst, C., Bingert, J., 2013. Modeling void growth in polycrystalline materials. Acta Mater. 61, 6918–6932.

Lebensohn, R., Montagnat, M., Mansuy, P., Duval, P., Meysonnier, J., Philip, A., 2009. Modeling viscoplastic behavior and heterogeneous intracrystalline deformation of columnar ice polycrystals. Acta Mater. 57, 1405–1415.

Lebensohn, R. A., Castelnau, O., Brenner, R., Gilormini, P., 2005. Study of the antiplane deformation of linear 2-D polycrystals with different microstructures. International Journal of Solids and Structures 46, 3018–3026.

Lebensohn, R. A., Idiart, M. I., Ponte-Castañeda, Vincent, P. G., 2011. Dilatational viscoplasticity of polycrystalline solids with intergranular cavities. Philosophical Magazine 91, 3038–3067.

Lebensohn, R. A., Kanjarla, A. K., Eisenlohr, P., 2012. An elasto-viscoplastic formulation based on Fast Fourier Transforms for the prediction of micromechanical fields in polycrystalline materials. International Journal of Plasticity 32-33, 59–69.

Lebensohn, R. A., Needleman, A., 2016. Numerical implementation of non-local polycrystal plasticity using fast Fourier transforms. J. Mech. Phys. Solids 97, 333–351.

Lee, S. B., Lebensohn, R. A., Rollett, A. D., 2011. Modeling the viscoplastic micromechanical response of two-phase materials using Fast Fourier Transforms. International Journal of Plasticity 27, 707–727.

Li, J., Tian, X. X., Abdelmoula, R., 2012. A damage model for crack prediction in brittle and quasi-brittle materials solved by the FFT method. International Journal of Fracture 173, 135–146.

Lloyd, D. J., 1994. Particle reinforced aluminium an magnesium matrix composites. Int. Metall. Rev. 39, 1–23.

Lucarini, S., Segurado, J., 2018. On the accuracy of spectral solvers for micromechanics based fatigue modeling. Computational Mechanics In Press, doi: 10.1007/s00466-018-1598-1.

Mecking, H., Kocks, U. F., 1981. Kinetics of flow and strain-hardening. Acta Metallurgica 29, 1865–1875.

Michel, J. C., Moulinec, H., Suquet, P., 1999. Effective properties of composite materials with periodic microstructure: a computational approach. Comp. Meth. Appl.

Mech. Eng. 172, 109–143.

Michel, J. C., Moulinec, H., Suquet, P., 2001. A computational scheme for linear and non-linear composites with arbitrary phase contrast. International Journal of Numerical Methods Engineering 52, 139–160.

Mika, D. P., Dawson, P. R., 1998. Effects of grain interaction on deformation in polycrystals. Materials Science Engineering A 257, 62–76.

Monchiet, V., Bonnet, G., 2013. Numerical homogenization of nonlinear composites with a polarization-based FFT iterative scheme. Comp. Mater. Sci. 79, 276–283.

Moulinec, H., Suquet, P., 1994. A fast numerical method for computing the linear and non linear properties of composites. Comptes Rendus de l'Académie des Sciences de Paris II 318, 1417–1423.

Moulinec, H., Suquet, P., 1998. A numerical method for computing the overall response of nonlinear composites with complex microstructure. Comput. Meth. Appl. Mech. Eng. 157, 69–94.

Mülhaus, H. B., Aifantis, E. C., 1991. A variational principle for gradient plasticity. International Journal of Solids and Structures 28, 845–857.

Müller, W., 1996. Mathematical vs. experimental stress analysis of inhomogeneities in solids. Journal of Physics IV 6 (C1), 139–148.

Müller, W., 1998. Fourier transforms and their application to the formation of texture and changes of morphology in solids, in: iutam Edition. Kluwer Academic Publishers.

Mura, T., 1963. Continuous distribution of moving dislocations. Philosophical Magazine 89, 843–857.

Mura, T., 1964. Periodic distributions of dislocations. Proc. Roy. Soc. London A 280, 528–544.

Mura, T., 1987. Micromechanics of defects in solids, dordrecht, Edition. Kluwer Academic Plublishers.

Nan, C. W., Clarke, D. R., 1996. The influence of particle size and particle fracture on the elastic/plastic deformation of metal matrix composites. Acta Mater. 44, 3801–3811.

Nye, J. F., 1953. Some geometrical relations in dislocated crystals. Acta Materialia 1, 153–162.

Otsuka, T., Brenner, R., Bacroix, B., 2018. FFT-based modelling of transformation plasticity in polycrystalline materials during diffusive phase transformation. International Journal of Engineering Sciences 127, 92–113.

Pardoen, T., Massart, T. J., 2012. Interface controlled plastic flow modeled by strain gradient plasticity theory. Comptes Rendus Mecanique 340, 247–260.

Prakash, A., Lebensohn, R., 2009. Simulation of micromechanical behavior of polycrystals : finite elements versus fast Fourier transforms. Modell. Simul. Mater. Sci. Eng. 17, 64010–64016.

Puri, S., Acharya, A., Rollett, A. D., 2010. Controlling plastic flow across grain boundaries in a continuum model. Metallurgical and Materials Transactions A 42, 669–675.

Puri, S., Das, A., Acharya, A., 2011. Mechanical response of multicrystalline thin films in mesoscale field dislocation mechanics. Journal of the Mechanics and Physics of Solids 59, 2400–2417.

Puri, S., Roy, A., 2012. Plastic deformation of multicrystalline thin films: Grain size distribution vs. grain orientation. Computational Materials Science 52, 20–24.

Puri, S., Roy, A., Acharya, A., Dimiduk, D., 2009. Modeling dislocation sources and size effects at initial yield in continuum plasticity. Journal of Mechanics of Materials and Structures 4 (9), 1603–1618.

Richards, A. W., Lebensohn, R. A., Bhattacharya, K., 2013. Interplay of martensitic phase transformation and plastic slip in polycrystals. Acta Materialia 61, 4384–4397.

Richeton, T., Le, L. T., Chauve, T., Bernacki, M., Berbenni, S., Montagnat, M., 2017. Modelling the transport of geometrically necessary dislocations on slip systems: application to single and multi-crystals of ice. Modelling and Simulation in Materials Science and Engineering 25, 025010(27pp).

Richeton, T., Wang, G. F., Fressengeas, C., 2011. Continuity constraints at the interfaces and their consequences on the work hardening of metal-matrix composites. Journal of the Mechanics and Physics of Solids 59, 2023–2043.

Rollett, A. D., Lebensohn, R. A., Groeber, M., Choi, Y., J., L., Rohrer, G. S., 2010. Stress hot spots in viscoplastic deformation of polycrystals. Modell. Simul. Mater. Sci. Eng. 18, 074005.

Roters, F., Eisenlohr, P., Hantcherli, L., Tjahjanto, D. D., Raabe, D., 2010. Overview of constitutive laws, kinematics, homogenization and multiscale methods in crystal plasticity finite-element modeling: Theory, experiments, applications. Acta Materialia 58, 1152–1211.

Rovinelli, A., Guilhem, Y., Proudhon, H., Lebensohn, R. A., Ludwig, W., Sangid, M. D., 2017a. Assessing reliability of fatigue indicator parameters for small crack growth via a probabilistic framework. Modell. Simul. Mater. Sci. Eng. 25, 045010.

Rovinelli, A., Proudhon, H., Lebensohn, R. A., , Sangid, M. D., 2012. Assessing the reliability of Fast Fourier Transform-based crystal plasticity simulations of a polycrystalline material near a crack tip. Comp. Meth. Appl. Mech. Eng., In Press.

Rovinelli, A., Sangid, M. D., Proudhon, H., Guilhem, Y., Lebensohn, R. A., Ludwig, W., 2017b. Predicting the 3-D fatigue crack growth rate of short cracks using multimodal data via Bayesian network: in-situ experiments and crystal plasticity simulations. Journal of the Mechanics and Physics of Solids 115, 208–229.

Roy, A., Acharya, A., 2005. Finite element approximation of field dislocation mechanics. J. Mech. Phys. Solids 53, 143–170.

Roy, A., Acharya, A., 2006. Size effects and idealized dislocation microstructure at small scales : Predictions of a Phenomenological model of Mesoscopic Field Dislocation Mechanics : Part II. Journal of the Mechanics and Physics of Solids 54, 1711–1743.

Roy, A., Puri, S., Acharya, A., 2007. Phenomenological mesoscopic field dislocation mechanics, lower-order gradient plasticity, and transport of mean excess dislocation density. Model. Simul. Mater. Sci. Eng. 15, 167–180.

Schneider, M., 2017. An FFT-based fast gradient method for elastic and inelastic unit cell homogenization problems. Comp. Meth. Appl. Mech. Eng. 315, 846–866.

Shanthraj, P., Eisenlohr, P., Diehl, M., Roters, F., 2015. Numerically robust spectral methods for crystal plasticity simulations of heterogeneous materials. International Journal of Plasticity 66, 31–45.

Sharma, L., Peerlings, R. H. J., Shanthraj, P., , Roters, F., Geers, M. G. D., 2012. FFT-based interface decohesion modelling by a nonlocal interphase. Adv. Model. Simul. Eng. Sci. 5, 7.

Shu, J. Y., Fleck, N. A., VanderGiessen, E., Needleman, A., 2001. Boundary layers in constrained plastic flow: comparison of nonlocal and discrete dislocation plasticity. Journal of the Mechanics and Physics of Solids 49, 1361–1395.

Suquet, P., Moulinec, H., Castelnau, O., Montagnat, M., Lahellec, N., Grennerat, F., Duval, P., Brenner, R., 2012. Multi-scale modeling of the mechanical behavior of polycrystalline ice under transient creep. Procedia IUTAM 3, 76–90.

Taupin, V., Berbenni, S., Fressengeas, C., 2012. Size effects on the hardening of channel-type microstructures: a field dislocation mechanics-based approach. Acta Materialia 60, 664–673.

Taupin, V., Varadhan, S., Chevy, J., Fressengeas, C., Beaudoin, A. J., Montagnat, M., Duval, P., 2007. Effects of size on the dynamics of dislocations in ice single crystals. Physical Review Letters 99, 155507.

Taupin, V., Varadhan, S., Fressengeas, C., Beaudoin, A. J., 2008. Directionality of yield point in strain-aged steels: the role of polar dislocations. Acta Materialia 56, 3002–3010.

Upadhyay, M. V., Capolungo, L., Taupin, V., Fressengeas, C., Lebensohn, R. A., 2016. A higher order elasto-viscoplastic model using fast fourier transforms: Effects of lattice curvatures on mechanical response of nanocrystalline metals. Int. J. Plast. 83, 126–152.

Varadhan, S., Baudoin, A. J., Acharya, A., Fressengeas, C., 2006. Dislocation transport using Galerkin/least squares formulation. Modelling and Simulation in Materials Science and Engineering 14, 1245–1270.

Varadhan, S., Beaudoin, A. J., Fressengeas, C., 2009. Lattice incompatibility and strain-aging in single crystals. Journal of the Mechanics and Physics of Solids 57, 1733–1748.

Vidyasagar, A., Tutcuoglu, A. D., Kochmann, D. M., 2018. Deformation patterning in finite-strain crystal plasticity by spectral homogenization with application to magnesium. Comp. Meth. Appl. Mech. Eng. 335, 584–609.

Vinogradov, V., Milton, G. W., 2008. An accelerated FFT algorithm for thermoelastic and non-linear composites. Int. J. Num. Meth. Eng. 76, 1678–1695.

Volterra, S., 1907. Sur l'équilibre des corps élastiques multiplement connexes. Annales Scientifiques de l'Ecole Normale Supérieure III 24, 401–517.

Willis, J. R., 1967. Second-order effects of dislocations in anisotropic ccrystals. International Journal of Engineering Sciences 5, 171–190.

Willot, F., 2015. Fourier-based schemes for computing the mechanical response of composites with accurate local fields. Comptes Rendus Mecanique 343, 232–245.

Willot, F., Pellegrini, Y. P., 2008. Fast Fourier transform computations and build-up of plastic deformation in 2D, elastic-perfectly plastic, pixelwise disordered porous media. Continuum Models and Discrete Systems, D. Jeulin and S. Forest (eds.),

CMDS11, Ecole des Mines Paris, 443–449.

Wulfinghoff, S., Forest, S., Böhlke, T., 2015. Strain gradient plasticity modeling of cyclic behavior of laminate structures. Journal of the Mechanics and Physics of Solids 79, 1–20.